Cellular/Molecular

Npas1$^+$-Nkx2.1$^+$ Neurons Are an Integral Part of the Cortico-pallido-cortical Loop

Zachary A. Abecassis,[1]* Brianna L. Berceau,[1]* Phyo H. Win,[1] Daniela García,[1] Harry S. Xenias,[1] Qiaoling Cui,[1] Arin Pamukcu,[1] Suraj Cherian,[1] Vivian M. Hernández,[1] Uree Chon[2], Byung Kook Lim,[3] Yongsoo Kim,[2] Nicholas J. Justice,[4,5] Raj Awatramani,[6] Bryan M. Hooks,[7] Charles R. Gerfen,[8] Simina M. Boca,[9] and C. Savio Chan[1]

[1]Department of Physiology, Feinberg School of Medicine, Northwestern University, Chicago, Illinois, [2]Department of Neural and Behavioral Sciences, College of Medicine, Pennsylvania State University, Hershey, Pennsylvania, [3]Neurobiology Section, Biological Sciences Division, University of California San Diego, La Jolla, California, [4]Center for Metabolic and degenerative disease, Institute of Molecular Medicine, University of Texas, Houston, Texas, [5]Department of Integrative Pharmacology, University of Texas, Houston, Texas, [6]Department of Neurology, Feinberg School of Medicine, Northwestern University, Chicago, Illinois, [7]Department of Neurobiology, University of Pittsburgh School of Medicine, Pittsburgh, Pennsylvania, [8]Laboratory of Systems Neuroscience, National Institute of Mental Health, Bethesda, Maryland, and [9]Innovation Center for Biomedical Informatics, Georgetown University Medical Center, Washington, District of Columbia

Within the basal ganglia circuit, the external globus pallidus (GPe) is critically involved in motor control. Aside from Foxp2$^+$ neurons and ChAT$^+$ neurons that have been established as unique neuron types, there is little consensus on the classification of GPe neurons. Properties of the remaining neuron types are poorly defined. In this study, we leverage new mouse lines, viral tools, and molecular markers to better define GPe neuron subtypes. We found that Sox6 represents a novel, defining marker for GPe neuron subtypes. Lhx6$^+$ neurons that lack the expression of Sox6 were devoid of both parvalbumin and Npas1. This result confirms previous assertions of the existence of a unique Lhx6$^+$ population. Neurons that arise from the Dbx1$^+$ lineage were similarly abundant in the GPe and displayed a heterogeneous makeup. Importantly, tracing experiments revealed that Npas1$^+$-Nkx2.1$^+$ neurons represent the principal noncholinergic, cortically-projecting neurons. In other words, they form the pallido-cortical arm of the cortico-pallido-cortical loop. Our data further show that pyramidal-tract neurons in the cortex collateralized within the GPe, forming a closed-loop system between the two brain structures. Overall, our findings reconcile some of the discrepancies that arose from differences in techniques or the reliance on preexisting tools. Although spatial distribution and electrophysiological properties of GPe neurons reaffirm the diversification of GPe subtypes, statistical analyses strongly support the notion that these neuron subtypes can be categorized under the two principal neuron classes: PV$^+$ neurons and Npas1$^+$ neurons.

Key words: arkypallidal neurons; basal ganglia; cellular diversity; globus pallidus; pallidocortical neurons; prototypic neurons

Significance Statement

The poor understanding of the neuronal composition in the external globus pallidus (GPe) undermines our ability to interrogate its precise behavioral and disease involvements. In this study, 12 different genetic crosses were used, hundreds of neurons were electrophysiologically characterized, and >100,000 neurons were histologically- and/or anatomically-profiled. Our current study further establishes the segregation of GPe neuron classes and illustrates the complexity of GPe neurons in adult mice. Our results support the idea that Npas1$^+$–Nkx2.1$^+$ neurons are a distinct GPe neuron subclass. By providing a detailed analysis of the organization of the cortico-pallidal-cortical projection, our findings establish the cellular and circuit substrates that can be important for motor function and dysfunction.

Introduction

The basal ganglia are a network of brain nuclei that are involved in motor control and adaptive behavior. Dysfunction within this

Received May 22, 2019; revised Nov. 21, 2019; accepted Nov. 26, 2019.

Author contributions: Z.A.A. and B.L.B. conceived the study; Z.A.A., H.S.X., Q.C., A.P., S.C., and V.M.H. conducted and analyzed the electrophysiological measurements; D.G., P.H.W., Z.A.A., Q.C., and B.L. examined the anatomical GPe projections; U.C., B.L., Y.K., B.M.H., and C.R.G. studied the organization of the cortico-pallidal projection; B.L.B. performed the immunohistological experiments and confocal imaging; P.H.W. performed cell counts and generated spatial maps; H.S.X. led the effort in data analysis and visualization using MATLAB; H.S.X. and Q.C. provided technical and analytical training; S.M.B. performed logistic regression analysis and oversaw all statistical analyses in this study; N.J.J. and R.A. provided unpublished data and reagents that led to the proposed classification scheme; B.L.B. led the writing of the manuscript with input from all co-authors; C.S.C. designed, directed, and supervised the project; All authors reviewed and edited the manuscript.

This work was supported by the National Institutes of Health (Grants R01 NS069777 to C.S.C., P50 NS047085 to C.S.C., R01 MH112768 to C.S.C., R01 NS097901 to C.S.C., R01 MH109466 to C.S.C., R01 NS088528 to C.S.C., R01 NS096240 to R.A., R01 MH110556 to R.A., P50 DA044121 to R.A., R01 MH107742 to B.L., R01 MH108594 to B.K.L.,

circuit can be devastating, as seen in patients afflicted with Parkinson's disease (PD), Huntington's disease, and dystonias (DeLong and Wichmann, 2007; Graybiel, 2008; Pennartz et al., 2009; Redgrave et al., 2010; Ito and Doya, 2011; Nambu and Tachibana, 2014; Jahanshahi et al., 2015; Dudman and Krakauer, 2016; Grillner and Robertson, 2016; Mink, 2018; Cox and Witten, 2019; Klaus et al., 2019). The external globus pallidus (GPe) is a key nucleus within the basal ganglia. Decorrelated, phasic changes in GPe neuron activity are observed with normal movements (Anderson and Horak, 1985; Shi et al., 2004; Turner and Anderson, 2005; Jin et al., 2014; Dodson et al., 2015; Mallet et al., 2016). Alterations in the firing pattern of these neurons are associated with hypokinetic motor symptoms in both animal models of PD and human patients (Filion et al., 1991; Hutchison et al., 1994; Nini et al., 1995; Rothblat and Schneider, 1995; Boraud et al., 1998; Raz et al., 2000; Magill et al., 2001; Mallet et al., 2008; Chan et al., 2011; Jaeger and Kita, 2011).

Prior studies in the field have suggested GPe neuron subtypes are involved in some aspects of movement control (Dodson et al., 2015; Glajch et al., 2016; Mastro et al., 2017). However, precisely how these neuron subclasses are involved in motor function and dysfunction remains poorly defined. Our past work characterized two principal classes of GPe neurons, parvalbumin-expressing (PV$^+$) neurons and Npas1-expressing (Npas1$^+$) neurons, which account for 55% and 27% of the GPe neurons, respectively. PV$^+$ neurons project primarily to the subthalamic nucleus (STN) and Npas1$^+$ neurons target the dorsal striatum (dStr). The Npas1$^+$ population can be further broken down into distinct Foxp2-expressing (Foxp2$^+$) and Nkx2.1-expressing (Nkx2.1$^+$) subpopulations, with Foxp2$^+$ neurons representing a unique population referred to as "arkypallidal" neurons (Abdi et al., 2015; Dodson et al., 2015; Hernández et al., 2015). GPe neurons lacking Foxp2 expression, commonly referred to as "prototypic" neurons, are a more heterogeneous population. As we lack a complete description of the molecular identity of prototypic neurons, the precise function of prototypic neurons has not been systematically studied.

Lhx6-expressing (Lhx6$^+$) neurons represent a substantial fraction of the prototypic GPe neuron subtype, although their reported abundance varies widely across laboratories (Mastro et al., 2014; Dodson et al., 2015; Hernández et al., 2015; Abrahao and Lovinger, 2018). Unfortunately, due to limitations in the availability of a reliable transgenic mouse and antibodies to study this subset, a discrepancy remains in its abundance and extent of overlap with PV$^+$ neurons and Npas1$^+$ neurons across laboratories (Hegeman et al., 2016). In this study, we hypothesize the existence of a unique Lhx6$^+$ GPe population that corresponds to the PV$^-$ and Npas1$^-$ (PV$^-$-Npas1$^-$) neurons we previously identified and accounts for ~15–20% of the total GPe neuron population (Hernández et al., 2015). These neurons could play an important role in neural function if they target a unique brain area, such as the cortex, which has been described (Van der Kooy and Kolb, 1985; Chen et al., 2015; Saunders et al., 2015; Schwarz et al., 2015; Ährlund-Richter et al., 2019; Sun et al., 2019). With the advent of additional transgenic lines and viruses, we used molecular marker expression and connectome analysis to reconcile discrepancies and provide a more in-depth analysis of the neuronal makeup and its diversity within the GPe. We confirmed the existence of a unique Lhx6$^+$ neuron population by its lack of Sox6 expression. This Lhx6$^+$ population does not correspond to neurons that arise from the Dbx1-lineage, which is known to colonize the GPe. We found that Npas1$^+$-Nkx2.1$^+$ neurons represent the principal, noncholinergic, cortically-projecting population, and they are part of a closed-loop formed between cortex and the GPe. We propose that Npas1$^+$-Nkx2.1$^+$ neurons, along with the previously identified Npas1$^+$-Foxp2$^+$ and ChAT$^+$ neurons, are unique GPe neuron types.

Materials and Methods

Mice. All procedures were done in accordance with protocols approved by Northwestern University, the University of California at San Diego, the University of Pittsburgh, and the Janelia Research Campus Institutional Animal Care and Use Committees and were in compliance with the National Institutes of Health's *Guide to the Care and Use of Laboratory Animals*. Experiments were conducted with the following mouse lines: LSL(Lox-STOP-Lox)-tdTomato (Ai14, Jax 007914), FSF(Frt-STOP-Frt)-LSL-tdTomato (Ai65, Jax 021875). Dbx1-Cre (Dbx1-ires-Cre, MMRRC 031751) (Harris et al., 2014) were crossed with LSL-tdTomato. As the Dbx1-Cre line is prone to germline recombination, recombination patterns were routinely monitored and compared against data on Allen's Transgenic Characterization data portal (http://connectivity.brain-map.org/transgenic/experiment/100141723). Any mice displaying ectopic expression were excluded from subsequent analysis. Emx1-Cre (Emx1-ires-Cre, Jax 005628), Foxp2-Cre (Foxp2-ires-Cre, Jax 030541), Lhx6-GFP (Lhx6-GFP BAC, MMRRC 000246), Nkx2.1-Flp (Nkx2.1-ires-Flp, Jax 028577), Npas1-Cre-tdTom (Npas1-Cre-tdTomato BAC, Jax 027718), PV-Cre (PV-ires-Cre, Jax 017320), PV-Flp (PV-2A-Flp, Jax 022730), PV-tdTom (PV-tdTomato BAC, Jax 027395), Sim1-Cre (Sim1-Cre BAC, MMRRC 037650) and Tlx3-Cre (Tlx3-Cre BAC, MMRRC 036670) were all used in this study. FSF-tdTomato (Ai65F) was generated as previously described (Daigle et al., 2018; Yetman et al., 2019). In brief, FSF-LSL-tdTomato was crossed with EIIa-Cre (Jax 003724) to delete the LSL cassette. Sox6-Cre was generated by performing a germline deletion of the FSF cassette from our previously reported Sox6-FSF-Cre (Poulin et al., 2018), using CAG-Flp (Kanki et al., 2006) line. Dbx1;Ai14 referred to as Dbx1-L-tdTom. Nkx2.1-Flp;Ai65 referred to as Nkx2.1-F-tdTom. PV-Cre;Ai14 referred to as PV-L-tdTom. PV-Flp;Ai65F referred to as PV-F-tdTom. PV-Flp;Dbx1-Cre;Ai65 referred to as PV-Dbx1-FL-tdTom. Mice were backcrossed and only heterozygous and hemizygous mice were used throughout the study to minimize the potential alteration of the phenotypes in mice carrying the transgene alleles (Chan et al., 2012). Mice were group-housed in a 12 h light–dark cycle. Food and water were provided *ad libitum*. All mice were maintained by backcrossing with C57BL/6J breeders (Jax 000664). The genotypes of all transgenic mice were determined by tail biopsy followed by PCR to identify the presence of the relevant transgenes. Both male and female mice were used in this study.

Stereotaxic injections. Standard injection procedures were used as described previously (Cui et al., 2016). In brief, mice at postnatal days 28–35 and 45–55 were used for viral tracing and retrograde tracing experiments, respectively, were anesthetized with isoflurane, and were immobilized on a stereotaxic frame (David Kopf Instruments). A small craniotomy (~1 mm diameter) was made with a dental drill (Osada) for injection into the target (Table 1) using a calibrated glass micropipette (VWR) at a rate of 0.3–0.5 μl/min. The micropipette was left *in situ* for 5–10 min postinjection to maximize viral retention and to decrease capillary spread upon pipette withdrawal. The following adeno-associated viruses (AAVs) were used in this study: AAV-EF1a-CreOn-hChR2 (H134R)-EYFP (Addgene viral prep #20298-AAV9) and AAV-

U01 MH114829 to B.K.L., R01 MH116176 to Y.K., R01 MH112768 to N.J.J., R56 MH114032 to N.J.J., R21 AA026022 to N.J.J., R01 NS103993 to B.M.H., ZIA MH002497 to C.R.G., T32 NS041234 to H.S.X., F32 NS098793 to H.S.X., and T32 AG020506 to A.P.), a NARSAD Young Investigator Award to B.M.H., a Howard Hughes Medical Institute HHMI-PF Medical Research Fellowship to Z.A.A., an AΩA Student Research Fellowship to Z.A.A., and a Northwestern University Weinberg Summer Research Grant to P.H.W. We thank Xixun Du, Yu Zhang, Vishnu Rangachari, Kris Shah, Elizabeth Augustine, and Daniel Hegeman for assistance on the project; Alexandria Granados, Morgan Marshall, and Nicole Curtis for colony management and technical support; Alicia Guemez-Gamboa for providing Emx1-Cre mice; Jeffrey Savas for providing VGluT1 antibody; and the Northwestern University Transgenic and Targeted Mutagenesis Laboratory for providing EIIa-Cre and CAG-Flp breeders.

The authors declare no competing financial interests.

*Z.A.A. and B.L.B. contributed equally to this work.

Correspondence should be addressed to C. Savio Chan at saviochan@gmail.com.

https://doi.org/10.1523/JNEUROSCI.1199-19.2019

Table 1. Injection coordinates

	P28–P35				P45–P55		
	Injection volume (nl)	AP (mm)	ML (mm)	DV (mm)	AP (mm)	ML (mm)	DV (mm)
Primary somatosensory, primary somatomotor (SSp, MOp)	180	+2.60	±2.16	−2.55, −2.75	+2.60	±2.16	−2.25, −2.50
Secondary somatomotor (MOs), rostral	180	+1.80	±0.96	−1.20, −1.60	+2.60	±2.04	−2.55, −2.75
Secondary somatomotor (MOs), caudal	–	–	–	–	+1.80	±0.96	−1.20, −1.60
Anterior cingulate cortex (AC)	90	–	–	–	+1.00	±0.40	−1.60
Agranular cortex (AG)	180	+2.25	±1.92	−2.25, −3.00	−2.60	±2.04	−2.55, −2.75
Dorsal striatum (dStr)	180	+0.70	±2.30	−3.00, −3.40	+0.70	±2.30	−3.00, −3.40
External globus pallidus (GPe)	90	−0.28	±2.15	−4.10	−0.28	±2.15	−4.10
Subthalamic nucleus (STN)	90	−1.45	±1.70	−4.52	−1.45	±1.70	−4.53
Substantia nigra (SN)	180	−2.65, −3.00	±1.50	−4.50	−2.95	±1.44	−4.50
Parafascicular nucleus (Pf)	90	−2.10	±0.64	−3.50	−2.15	±0.64	−3.50

Coordinates are in relation to bregma. Negative AP values refer to coordinates caudal to bregma. AP, Anterior–posterior; ML, medial–lateral; DV, dorsal–ventral.

Table 2. Primary antibodies used in this study

Antigen	Host species	Clonality	Source	Catalog no.	Lot. no.	Dilution	Working concentration
ChAT	Gt	Polyclonal	Millipore-Sigma	AB144P	2916187	1:1000	
ChAT	Rb	Polyclonal	Synaptic Systems	297013	297013/3	1:2000	0.5 μg/ml
Cre	Rb	Polyclonal	Synaptic Systems	257003	257003/1–7	1:500	2.0 μg/ml
CTb	Gt	Polyclonal	List Biological Labs	102946–502	7032A10	1:5000–1:10000	
DsRed	Rb	Polyclonal	Clontech	632496		1:500–1:1000	
Foxp2	Ms	Monoclonal	Millipore-Sigma	MABE415	Q2273099	1:500	1.0 μg/ml
Foxp2	Rb	Monoclonal	Millipore-Sigma	ABE73	3037985	1:500	
Foxp2	Rb	Polyclonal	Millipore-Sigma	HPA000382	B115858	1:500	
GFP	Ck	Polyclonal	Abcam	ab13970	GR3190550–9	1:1000	
HuC/D	Ms	Monoclonal	Life Technologies	A21271	1900217	1:1000	0.2 μg/ml
mCherry	Rt	Monoclonal	Life Technologies	M11217	S1259077	1:1000–1:5000	0.4–2.0 μg/ml
NeuN	Rb	Polyclonal	Biosensis	R–3770–100	R-3770–300-201605-SH	1:1000	1.0 ng/μl
Nkx2.1	Rb	Polyclonal	Millipore-Sigma	07–601	2887266	1:500	
Npas1[a]	Gp	Polyclonal				1:5000	
Npas1[a]	Rb	Polyclonal				1:5000	
Parvalbumin	Ms	Monoclonal	Millipore-Sigma	P3088	016M-4847V	1:500	10.0 μg/ml
Parvalbumin	Ck	Polyclonal	Synaptic Systems	195006	195006/2	1:2000	
Parvalbumin	Gp	Polyclonal	Synaptic Systems	195004	195004/1–19	1:1000–1:2000	
Parvalbumin	Rb	Polyclonal	Swant	PV 27	2014	1:1000	
RFP	Ms	Monoclonal	Rockland	200–301–379	34537	1:1000	0.5 μg/ml
Sox6	Rb	Polyclonal	Abcam	ab30455	GR289554–2	1:5000	0.2 μg/ml
tdTomato	Rt	Monoclonal	Kerafast	EST203	091918	1:1000	0.5 μg/ml
VGluT1	Gp	Polyclonal	Millipore-Sigma	AB5905		1:1000	

[a]See Hernández et al., 2015.

Ck, Chicken; Gp, guinea pig; Gt, goat; Ms, mouse; Rb, rabbit; Rt, rat.

hSyn-CreOn-mCherry (Addgene viral prep #50459-AAV8) were used to infect GPe neurons. AAVretro-ChR2-eYFP (Addgene viral prep #20298-AAVrg) was used for retrograde delivery of ChR2 in Emx1-Cre mice. To examine cortical neuron subtype-specific projections, Tlx3-Cre and Sim1-Cre mice were injected at around postnatal day 37. 30 nl of AAV-flex-XFPs was injected per site. Mouse brains were then fixed by transcardial perfusion 2–3 weeks postinjection (Hooks et al., 2018). Mice injected with Alexa-conjugated cholera-toxin B subunit (CTb; Thermo Fisher Scientific), lentivirus (LVretro-Cre) (Knowland et al., 2017), or AAVs were processed for immunohistological analysis (see below) 7–14 d and 28–42 d after injection, respectively. For LV tracing experiments, CTb was injected in conjunction with LV to visualize targeting accuracy. Mice with injection outside of the targeted area were excluded from subsequent analysis.

Immunolabeling and quantification. Mice ranging in age from postnatal day 55 to 80 were anesthetized deeply with a ketamine–xylazine mixture and perfused transcardially first with PBS followed by fixative containing 4% paraformaldehyde (PFA, pH 7.4). Tissue was then post-fixed in the same fixative for 2 h at 4°C. Tissue blocks containing the GPe were sectioned using a vibrating microtome (Leica) at a thickness of 60 μm. Floating sections were blocked with 10% (v/v) normal goat or donkey serum (Thermo Fisher Scientific) and 0.2% (v/v) Triton X-100 in PBS for 30–60 min, and were subsequently incubated with primary antibodies (Table 2) in the same solution for 16–24 h at 4°C. After washes in PBS, the sections were incubated with Alexa Fluor-conjugated, secondary antibodies (Thermo Fisher Scientific, 1:500 dilution) at room temperature for 2 h. The sections were then washed, mounted with ProLong Antifade mounting medium (Thermo Fisher Scientific), and coverslipped. In a subset of the experiments, DAPI was used to delineate cytoarchitecture of different brain structures. Fluorescent images of injection sites were captured on an epifluorescence microscope (Keyence) using a 2× or 10× 0.45 numerical aperture (NA) objective. Immunoreactivity in neurons was examined on a laser-scanning confocal microscope (Olympus). For cell quantification, images of the entire GPe were acquired on a laser-scanning confocal microscope with a 60× 1.35 NA oil-immersion objective. Images encompassing the GPe were taken and stitched using FLUOVIEW Viewer (Olympus) or Photoshop (Adobe Systems). Cell counting was performed manually using the cell-counter plugin within Fiji (Schindelin et al., 2012). Cell counts were obtained from ~28 optical sections that were captured at 1 μm increments (median = 28). Neurons were defined by cells that were immunopositive for HuCD or NeuN (Hernández et al., 2015). GPe sections from three different equally spaced (400 μm) lateromedial levels (~2.5, 2.1, and 1.7 mm from bregma) were sampled and assigned as lateral, intermediate, and medial, respectively (Hernández et al., 2015). They correspond approximately to sagittal plate 7, 9, and 11 on the Allen reference atlas

(http://mouse.brain-map.org/static/atlas). In this study, the GPe is considered to be the structure that spans between the dorsal striatum and the internal capsule, which define the rostral and caudal and borders of the GPe on a sagittal plane, respectively. The cytoarchitecture of the ventral border is more ambiguous. For consistency, six nonoverlapping *z*-stacks (212.13 × 212.13 μm) traversing the long axis of the GPe were used to capture its dorsoventral extent. This strategy coincides with the ventral border demarcated by the dense astrocytic labeling in the Dbx1-L-tdTom mice (see Results) and that defined in the common reference atlas.

To mathematically represent the spatial distribution of GPe neurons and to compare that across neuron populations, sagittal brain sections were histologically processed. Images were manually aligned to the Allen Reference Atlas based on the structural information across the entire brain section. Images were transformed linearly (i.e., rotation, scaling) with no warping algorithms applied. Neurons that were not present within the confines of the GPe in the reference atlas were removed from subsequent analysis. GPe neurons located at lateral, intermediate, and medial levels (~2.5, 2.1, and 1.7 mm lateral from bregma) were charted and collapsed onto a single sagittal plane. The location of each neuron was then defined by its *x*–*y* coordinates. To capture the aggregate spatial distribution, a geometric centroid of each neuron population was then determined to represent the center of mass in both *x* and *y* dimensions. Centroids were then used as the origin for the polar histograms. The size of each sector represents the relative neuron count as a function of direction. Histological and analysis procedures for projections from cortical neuron subtypes have been described previously (Hooks et al., 2018).

Serial two-photon tomography. Serial two-photon tomography was used to map input to the GPe from the entire cortex. Imaging and analysis were performed as previously described (Kim et al., 2017). Two weeks after LVretro-Cre and CTb-488 injection, mouse brains were fixed as described above. Brains were then transferred to PBS and stored at 4°C until imaged. Brains were embedded in 4% agarose in 0.05 M phosphate buffer and cross-linked in 0.2% sodium borohydrate solution (in PBS, pH 9.0–9.5). Each brain was imaged with a high-speed two-photon microscope with integrated vibratome (TissueVision) at 1 μm at both *x*–*y* resolution with 280 *z*-sections in every 50 μm. A 910 nm two-photon laser (Coherent Technologies) was used for CTb-488 and tdTomato excitation. A dichroic mirror (Chroma) and band-pass filters (Semrock) were used to separate green and red fluorescence signals. Emission signals were detected by GaAsP photomultiplier tubes (Hamamatsu). An automated, whole-brain cell counting and registration of the detected signal on a reference brain was applied as described before (Kim et al., 2017). The number of tdTomato$^+$ neurons from each brain region was charted. The relative size of input to the GPe was calculated by normalizing the total number of tdTomato$^+$ neurons in the entire brain of each sample.

Visualized ex vivo *electrophysiology*. Mice in the age range postnatal day 55–90 were anesthetized with a ketamine-xylazine mixture and perfused transcardially with ice-cold aCSF containing the following (in mM): 125 NaCl, 2.5 KCl, 1.25 NaH_2PO_4, 2.0 $CaCl_2$, 1.0 $MgCl_2$, 25 $NaHCO_3$, and 12.5 glucose, bubbled continuously with carbogen (95% O_2 and 5% CO_2). The brains were rapidly removed, glued to the stage of a vibrating microtome (Leica), and immersed in ice-cold aCSF. Parasagittal slices containing the dStr and the GPe were cut at a thickness of 240 μm and transferred to a holding chamber where they were submerged in aCSF at 37°C for 30 min and returned to room temperature for recording. Slices were then transferred to a small-volume (~0.5 ml) Delrin recording chamber that was mounted on a fixed-stage, upright microscope (Olympus). Neurons were visualized using differential interference contrast optics (Olympus), illuminated at 735 nm (Thorlabs), and imaged with a 60× water-immersion objective (Olympus) and a CCD camera (QImaging). Genetically defined neurons were identified by somatic eGFP or tdTomato fluorescence examined under epifluorescence microscopy with a daylight (6500 K) LED (Thorlabs) and appropriate filters (Semrock).

Recordings were made at room temperature (20–22°C) with patch electrodes fabricated from capillary glass (Sutter Instrument) pulled on a Flaming-Brown puller (Sutter Instrument) and fire-polished with a microforge (Narishige) immediately before use. Pipette resistance was typically ~2–4 MΩ. For cell-attached and current-clamp recordings, the internal solution consisted of the following (in mM): 135 $KMeSO_4$, 10 Na_2phosphocreatine, 5 KCl, 5 EGTA, 5 HEPES, 2 Mg_2ATP, 0.5 $CaCl_2$, and 0.5 Na_3GTP, with pH adjusted to 7.25–7.30 with KOH. The liquid junction potential for this internal solution was ~7 mV and was not corrected. Stimulus generation and data acquisition were performed using an amplifier (Molecular Devices), a digitizer (Molecular Devices), and pClamp (Molecular Devices). For current-clamp recordings, the amplifier bridge circuit was adjusted to compensate for electrode resistance and was subsequently monitored. The signals were filtered at 1 kHz and digitized at 10 kHz. $KMeSO_4$ and Na_2-GTP were from ICN Biomedicals and Roche, respectively. All other reagents were obtained from Sigma-Aldrich.

For optogenetic experiments, blue excitation wavelength (peak, ~450 nm) from two daylight (6500 K) LEDs (Thorlabs) was delivered to the tissue slice from both a 60× water-immersion objective and a 0.9 numerical aperture air condenser with the aid of 520 nm dichroic beamsplitters (Semrock). Light delivery was made at the site of electrophysiological recordings with a field of illumination of 500–700 μm in diameter. Paired-pulse optogenetic activation of terminals was at 20 Hz with a light duration of 2 ms.

Experimental design and statistical analyses. General graphing and statistical analyses were performed with MATLAB (The MathWorks), Prism (GraphPad), and the R environment (https://www.r-project.org). Custom analysis codes are available on GitHub (https://github.com/chanlab). Sample size (*n* value) is defined by the number of observations (i.e., neurons, sections). When percentages are presented, *n* values represent only positive observations. No statistical method was used to predetermine sample size. All analyses are on the complete cases, not including imputation of any missing values. Data in the main text are presented as median values ± median absolute deviations (MADs) as measures of central tendency and statistical dispersion, respectively. Box plots are used for graphic representation of population data unless stated otherwise (Krzywinski and Altman, 2014; Streit and Gehlenborg, 2014). The central line represents the median, the box edges represent the interquartile ranges, and the whiskers represent 10–90th percentiles. Normal distributions of data were not assumed. Individual data points were visualized for small sizes or to emphasize variability in the data. For each characteristic, a Kruskal–Wallis test was performed to detect an overall difference between neuron types. Lhx6$^+$ neurons were considered together between all pairs of neuron types and evaluated using Dunn's test, and differences between the Lhx6$^+_{bright}$ and Lhx6$^+_{dim}$ subtypes and all other cell types were evaluated using the Mann–Whitney *U* test. Unless $<$ 0.0001, exact *p*-values (two-tailed) are reported. Given that multiple tests were performed, to maintain an overall family wise error rate of $\alpha = 0.05$, the Bonferroni approach was used for each of the three sets of statistical tests. *K*-means analysis was performed in MATLAB with the number of clusters varying from two to six, considering spontaneous rate and CV_{ISI} as the clustering variables. Principal component analysis was performed in ClustVis (https://biit.cs.ut.ee/clustvis/) (Metsalu and Vilo, 2015); all cell-attached and whole-cell measurements were included in this analysis. Both rows and columns were clustered using correlation distance and average linkage. Electrophysiological measurements were centered and scaled. The median differences in spontaneous rate between different neuron types and the PV$^+$ neurons and Npas1$^+$ neurons and their 95% confidence intervals were estimated using the Estimation Stats application (https://www.estimationstats.com); five thousand bootstrap samples were taken; bias-corrected and accelerated (BC_a) correction were applied to the resampling bootstrap distributions to adjust for both bias and skewness (Ho et al., 2019). Logistic regressions evaluating the correlation between the different variables and the Npas1$^+$ neurons and PV$^+$ neurons were also performed using the R programming language.

Results

PV$^+$ and Npas1$^+$ neurons are distinct GPe neuron classes

Our laboratory and others have shown previously that the GPe contains two principal, near-exclusive classes of neurons distinguished by their respective expression of PV and Npas1 (Hegeman et al., 2016). However, the reported abundance of PV$^+$

neurons across laboratories ranges from 30 to 60%, and their overlap with Npas1$^+$ neurons within the GPe varies widely in the literature (Flandin et al., 2010; Nóbrega-Pereira et al., 2010; Mastro et al., 2014; Abdi et al., 2015; Dodson et al., 2015; Saunders et al., 2015; Oh et al., 2017; Abrahao and Lovinger, 2018). As multiple mouse lines and well characterized antibodies are available to study PV$^+$ neurons, we sought to reevaluate the abundance of PV$^+$ GPe neurons and reconcile the inconsistencies. First, we examined PV immunoreactivity (PV-ir) across all GPe neurons using HuCD as a neuronal marker; we observed PV-ir in ~50% of GPe neurons (49 ± 4%, n = 2726 neurons, 19 sections) (Fig. 1*c*). Note that the range observed within the PV population data (Fig. 1*c*) mirrors the variance reported in the literature, suggesting that the discrepancy in the literature is likely of biological origin rather than methodological. Four PV antibodies were used throughout the study (Table 2). All PV antibodies yielded similar results and were therefore pooled. Although both PV-tdTom and PV-L-tdTom (PV-Cre;LSL-tdTomato) have been used consistently across laboratories for the identification of PV$^+$ neurons, the utility of the PV-Flp line for studies of GPe neurons had not been established. To harness the potential of this mouse line, we crossed it with a Flp-reporter (FSF-tdTomato) line (see Materials and Methods). The resultant PV-F-tdTom (PV-Flp;FSF-tdTomato) line produced robust, cytoplasmic neuron labeling similar to that of the PV-L-tdTom and PV-tdTom lines. As expected, the PV-F-tdTom line showed prominent tdTomato expression (tdTomato$^+$) not only in GPe PV$^+$ neurons but also in PV$^+$ neurons in the thalamic reticular nucleus (TRN) (Fig. 1*d*,*e*) and cerebellum, as well as in PV$^+$ interneurons throughout the cortex, hippocampus, and striatum.

Across the PV-tdTom, PV-L-tdTom, and PV-F-tdTom lines, the abundance of tdTomato$^+$ neurons converged to ~50% of the total GPe neuron population (PV-tdTom, 50 ± 9%, n = 571 neurons, 5 sections; PV-L-tdTom, 50 ± 13%, n = 848 neurons, 9 sections; PV-F-tdTom, 53 ± 15%, n = 859 neurons, 6 sections). Comparison of tdTomato expression with PV-ir demonstrated faithful reporting of PV$^+$ neurons in all three transgenic lines (PV-tdTom, 100 ± 0%, n = 742 of 747 neurons, 6 sections; PV-L-tdTom, 100 ± 0%, n = 1380 of 1392 neurons, 12 sections; PV-F-tdTom, 100 ± 0%, n = 930 of 1023 neurons, 6 sections).

The Npas1-Cre-tdTom line was previously generated in our laboratory and labels ~90% (88 ± 7%, n = 505 neurons) of neurons that endogenously express Npas1 in the GPe (Hernández et al., 2015). As this mouse line does not fully capture all Npas1$^+$ neurons, we focused our quantifications on Npas1-immunoreactivity (Npas1-ir) with our previously characterized Npas1 antibodies (Hernández et al., 2015). We found that Npas1$^+$ neurons make up ~30% (32 ± 4%, n = 3361 neurons, 21 sections) of all GPe neurons. This result is consistent with our previous quantification of 27% of the entirety of the GPe. A reevaluation of the overlap between PV and Npas1 confirmed our prior observation (Hernández et al., 2015) that these two markers are expressed in almost completely segregated neuron populations. We observed a very low level of overlap across lateromedial GPe levels (2 ± 2%, n = 96 of 1777 neurons, 12 sections), with the most overlap observed at the intermediate level (lateral: 1 ± 1%, n = 17 neurons, 3 sections; intermediate: 3 ± 1%, n = 68 neurons, 5 sections; medial: 0 ± 0%, n = 11 neurons, 4 sections). This is slightly higher than our previous estimate and may be related to our previous reliance on the Npas1 mouse line for quantification (Hernández et al., 2015). Our data are at odds with those of Abrahao and Lovinger (2018), which showed a much higher (up to 12.6%) overlap between PV and Npas1 expression in the GPe. This discrepancy can be attributed to differences in immunolabeling protocols, quantification methods, and the age of mice used in the experiments.

As determined by immunolabeling, a small population of neurons expressed a cholinergic neuron marker, choline acetyltransferase (ChAT) (6 ± 2%, n = 267 neurons, 9 sections), a finding that is consistent with our previous reports (Gritti et al., 2006; Nóbrega-Pereira et al., 2010; Hernández et al., 2015) (Table 3). This leaves ~15% of the GPe population that is unidentified by PV, Npas1, or ChAT.

Nkx2.1-F-tdTom mice label prototypic GPe neurons

Based on our previous data showing that Lhx6$^+$ neurons overlap substantially with both PV$^+$ neurons and Npas1$^+$ neurons (Hernández et al., 2015), we hypothesized that a subset of Lhx6$^+$ neurons may correspond to the 15% of GPe neurons that are PV$^-$ and Npas1$^-$ (and ChAT$^-$) (Fig. 1*f*). However, the use of the Lhx6-GFP mouse line has resulted in highly inconsistent results across laboratories (Hegeman et al., 2016).

To glean insights into an improved GPe neuron classification, we systematically examined the GPe expression of Nkx2.1 and Sox6, signaling molecules that are upstream and downstream of Lhx6, respectively. This was motivated by the observation that Nkx2.1, Lhx6, and Sox6 work in concert to control the fate of forebrain GABAergic neurons (Du et al., 2008; Batista-Brito et al., 2009; Jaglin et al., 2012). Consistent with the fact that Nkx2.1 plays a crucial role in GPe development (Rubenstein et al., 1998; Sussel et al., 1999; Flandin et al., 2010; Nóbrega-Pereira et al., 2010), Nkx2.1 immunolabeling revealed that ~60% (60 ± 2%, n = 5342 neurons, 16 sections) of GPe neurons are Nkx2.1-expressing (Nkx2.1$^+$) (Fig. 1*c*,*e*, Table 3). In keeping with our previous analysis of Lhx6 and Foxp2 (Hernández et al., 2015), we observed no overlap between Nkx2.1$^+$ neurons and Foxp2-expressing (Foxp2$^+$) neurons in wild-type brain sections (n = 1 of 1131 Nkx2.1$^+$ neurons, 3 sections; n = 1 of 414 Foxp2$^+$ neurons, 3 sections). Subsequent immunohistological analysis of Nkx2.1 antibody labeling with established GPe markers revealed that the majority of Nkx2.1$^+$ neurons are PV$^+$ (71 ± 3%, n = 1105 neurons, 7 sections), while a smaller subset are Npas1$^+$ (17 ± 2%, n = 383 neurons, 6 sections) or Lhx6$^+$ (41 ± 7%, n = 1469 neurons, 9 sections) (Table 3). Importantly, Nkx2.1$^+$ neurons are only ~80% (83 ± 4%, n = 1105 neurons, 7 sections) of PV$^+$ neurons, consistent with previous observations (Xu et al., 2008). Furthermore, Nkx2.1$^+$ neurons represent ~80% (78 ± 8%, n = 1469 neurons, 9 sections) of Lhx6$^+$ neurons and only a subset of Npas1$^+$ neurons (32 ± 1%, n = 383 neurons, 6 sections). More importantly, with triple immunostaining, we found that nearly all Npas1$^+$-Nkx2.1$^+$ neurons are Lhx6$^+$ (90 ± 5%, n = 184 of 204 neurons, 3 sections). Accordingly, the Npas1$^+$-Nkx2.1$^+$ and Npas1$^+$-Lhx6$^+$ populations of Npas1$^+$ neurons are near-identical (33 ± 5%, n = 204 of 609 neurons, 3 sections and 32 ± 3%, n = 233 of 609 neurons, 3 sections, respectively) (data not shown). This finding is in line with what we have described previously (Hernández et al., 2015).

To effectively identify all neurons derived from the Nkx2.1 lineage, we made a Nkx2.1-F-tdTom (Nkx2.1-Flp;FSF-tdTomato) genetic cross, which yielded robust tdTomato labeling (tdTomato$^+$) in the GPe. In addition to tdTomato$^+$ neurons, we observed tdTomato$^+$ glia in the GPe that were distinguished from neurons based on their morphology. To assess the cumulative recombination events in Nkx2.1-F-tdTom, we compared tdTomato expression to Nkx2.1 immunolabeling. Immunoreactivity on Nkx2.1-F-tdTom brain sections with tdTomato, Nkx2.1, and HuCD antibodies revealed ~90%

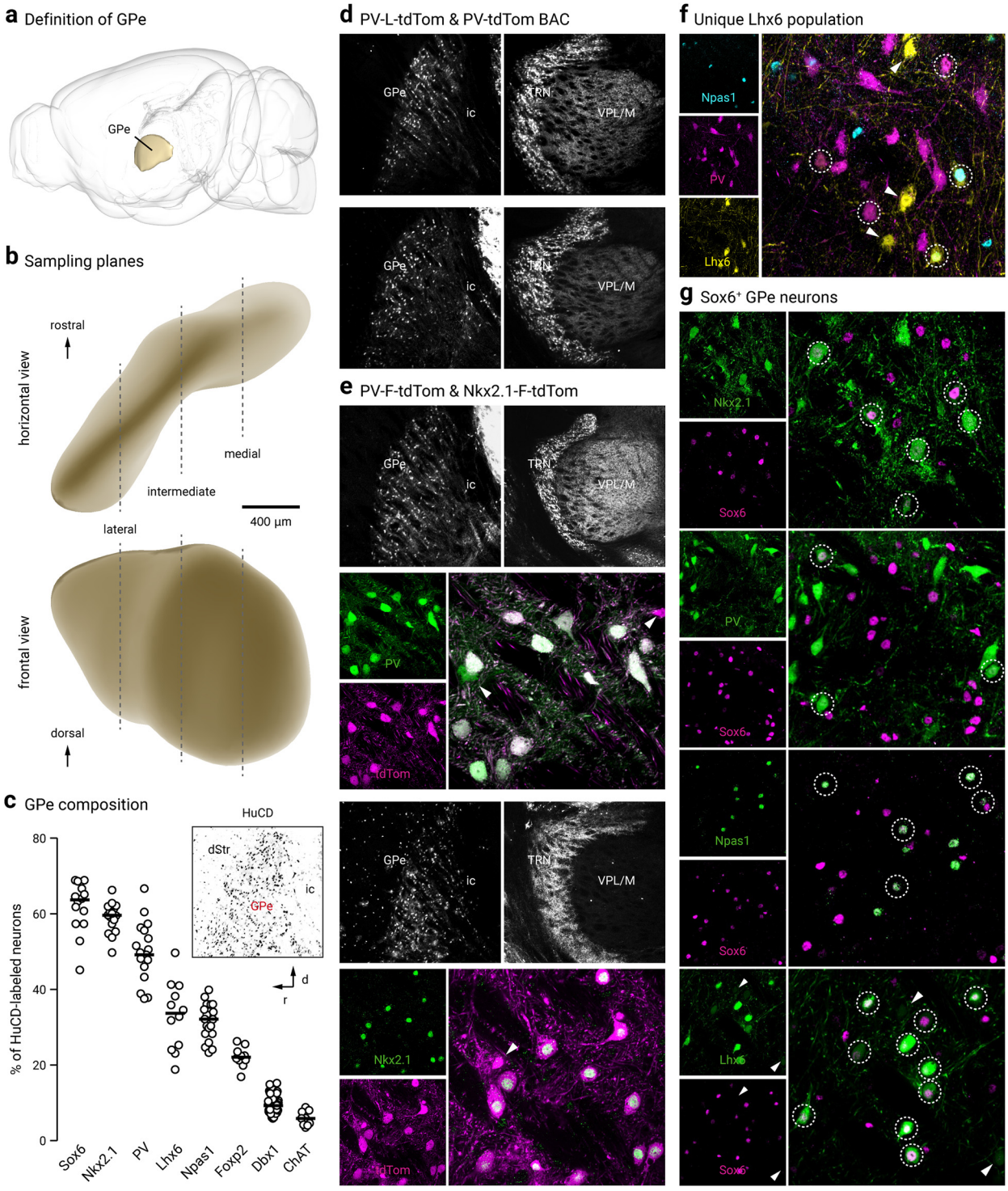

Figure 1. GPe neuron diversity. ***a***, The location of the GPe in a mouse brain is illustrated (side view). ***b***, GPe neurons at three different lateral, intermediate, and medial levels (~2.5, 2.1, and 1.7 lateral from bregma) were sampled. ***c***, Using HuCD as a neuronal marker, population data for the relative abundance of GPe neuron markers was determined. Each circle represents a section. Inset: low-magnification confocal image of a sagittal brain section showing HuCD-labeling in the GPe with the dStr and ic defining the rostral and caudal borders, respectively. Note the low density of HuCD-labeled cells outside of the GPe. ***d***, Low-magnification confocal images of the GPe and TRN in PV-L-tdTom (PV-Cre;LSL-tdTomato, top) and PV-tdTom (bottom) mice. ***e***, PV-F-tdTom (PV-Flp;FSF-tdTomato) and Nkx2.1-F-tdTom (Nkx2.1-Flp;FSF-tdTomato) were used in this study. The PV-F-tdTom (PV-Flp;FSF-tdTomato) transgenic mouse line produces faithful reporting of PV $^{+}$ neurons and similar cytoplasmic neuron labeling as the PV-L-tdTom and PV-tdTom lines (as shown in ***d***). Top, low-magnification showing the PV-F-tdTom line produces prominent tdTomato expression (tdTomato $^{+}$) in PV $^{+}$ neurons in the TRN in addition to the GPe. To confirm the validity of the mouse line, tdTomato expression was compared against PV immunostaining. A higher magnification of the GPe shows nearly all tdTomato $^{+}$ (magenta) neurons colocalize with PV-ir (green). Bottom, Nkx2.1-F-tdTom reliably captures neurons that arise from the Nkx2.1 lineage. Note that no cell bodies were found in the TRN (see also Fig. 5*c*). Double immunolabeling with tdTomato and Nkx2.1 demonstrated ~90% colocalization. Arrowheads indicate neurons that do not colocalize. ***f***, Triple immunostaining with PV, Npas1, and GFP on Lhx6-GFP brain sections confirmed the existence of a Lhx6 $^{+}$-PV $^{-}$-Npas1 $^{-}$ GPe population. Circles indicate Lhx6 $^{+}$ neurons that colocalize with either PV or Npas1. Arrowheads point to unique Lhx6 $^{+}$ neurons. Note that there are both bright and dim populations of Lhx6 $^{+}$ neurons. ***g***, Sox6 $^{+}$ neurons express established GPe markers. Note that there are both bright and dim populations of Sox6 $^{+}$ neurons. Bottom, arrowheads indicate Lhx6 $^{+}$-Sox6 $^{-}$ neurons. dStr = dorsal striatum; TRN, thalamic reticular nucleus; VPL/VPM, ventral posterior nucleus; ic, internal capsule.

Table 3. Quantification of GPe neurons

	Molecularly defined neuron subtypes															
	Sox6$^+$		Nkx2.1$^+$		PV$^+$		Lhx6$^+$		Npas1$^+$		Foxp2$^+$		Dbx1$^+$		ChAT$^+$	
	Median ± MAD	*n* (neurons; sections)	Median ± MAD	*n* (neurons; sections)	Median ± MAD	*n* (neurons; sections)	Median ± MAD	*n* (neurons; sections)	Median ± MAD	*n* (neurons; sections)	Median ± MAD	*n* (neurons; sections)	Median ± MAD	*n* (neurons; sections)	Median ± MAD	*n* (neurons; sections)
Total GPe neurons (%)	63.7 ± 4.0	4681; 14	59.6 ± 2.3	5342; 16	49.2 ± 4.3	2726; 19	33.7 ± 7.5	2533; 12	32.1 ± 3.9	3361; 21	22.1 ± 1.1	1273; 10	9.3 ± 1.3	3002; 61	5.9 ± 1.7	267; 9
Coexpression (%)																
Sox6	–	–	68.2 ± 0.5	681; 3	52.5 ± 8.4	1675; 15	[c]75.5 ± 7.2	2346; 15	93.4 ± 5.6	1999; 14	67.0 ± 4.3	206; 3	51.6 ± 8.2	442; 15	0.0 ± 0.0	0; 3
Nkx2.1	58.2 ± 0.3	681; 3	–	–	83.2 ± 3.5	1105; 7	78.4 ± 8.0	1469; 9	32.0 ± 1.4	383; 6	0.0 ± 0.0	1; 3	77.8 ± 10.2	329; 9	–	–
PV	36.4 ± 3.2	1675; 15	70.8 ± 3.0	1105; 7	–	–	[d]28.1 ± 7.3	654; 12	2.7 ± 2.7	96; 12	–	–	72.0 ± 8.3	493; 23	–	–
Lhx6	47.0 ± 6.7	2346; 15	40.6 ± 7.4	1469; 9	24.1 ± 9.6	654;12	–	–	40.7 ± 4.6	818; 12	1.3 ± 1.3	8; 3	–	–	50.0 ± 3.6	48; 3
Npas1	45.4 ± 5.7	1999; 14	17.3 ± 2.3	383; 6	2.0 ± 2.0	96; 12	[b]35.2 ± 5.1	818; 12	–	–	79.3 ± 3.8	566; 6	9.5 ± 5.2	72; 14	–	–
Foxp2	34.1 ± 5.7	206; 13	0.0 ± 0.0	1; 3	–	–	1.9 ± 0.5	8; 3	56.8 ± 4.2	566; 6	–	–	3.6 ± 1.9	13; 10	–	–
Dbx1	10.4 ± 3.2	411; 15	12.0 ± 1.3	329; 9	13.6 ± 3.0	493; 23	–	–	3.3 ± 1.8	72; 14	1.5 ± 0.6	13; 10	–	–	10.6 ± 4.2	34; 9
ChAT	0.0 ± 0.0	0; 3	–	–	–	–	[f]6.7 ± 0.6	48; 3	–	–	–	–	7.4 ± 3.3	34; 9	–	–

Lhx6+ neuron composition: $a + b + d + e = 100\%$.

[a]Lhx6$^+$-PV$^+$ = 28%.

[b]Lhx6$^+$-Npas1$^+$ = 35%.

[c]Lhx6$^+$-Sox6$^+$ = 76%.

[d]Lhx6$^+$-PV$^-$-Npas1$^-$-Sox6$^-$: $100\% - c = 24\%$.

[e]Lhx6$^+$-PV$^-$-Npas1$^-$-Sox6$^+$: $c - a - b = 13\%$.

[f]ChAT$^+$ neurons can be a portion of Lhx6$^+$-PV$^-$-Npas1$^-$-Sox6$^-$ neurons.

Lhx6$^+$-PV$^+$ and Lhx6$^+$-Npas1$^+$ neurons also express Sox6.

MAD, Median absolute deviation.

(89 ± 11%, $n = 795$ neurons, 3 sections) of tdTomato$^+$ neurons colocalized with Nkx2.1$^+$ neurons (Fig. 1*e*). Although we observed significant tdTomato$^+$ labeling throughout the entire cortex, Nkx2.1 immunoreactivity was absent. These data corroborate previous findings that Nkx2.1 is downregulated in cortical interneurons in adult mice (Butt et al., 2008; Nóbrega-Pereira et al., 2008) and that the majority of GPe neurons that are derived from the Nkx2.1 lineage maintain Nkx2.1 expression into adulthood. Similarly, we observed no tdTomato$^+$ or Nkx2.1$^+$ cell bodies in regions caudal to the forebrain, such as the TRN (Fig. 1*e*), STN, and SNr (data not shown).

Sox6 delineates GPe neuron subtypes

Previous literature demonstrates that the transcription factor Sox6 is present in most, if not all, medial ganglionic eminence (MGE)-derived neurons in the mature brain (Azim et al., 2009; Batista-Brito et al., 2009). Moreover, Sox6 and Lhx6 colocalize extensively within the MGE (Batista-Brito et al., 2009), consistent with the function of Sox6 as a downstream signaling partner of Lhx6 (Azim et al., 2009; Batista-Brito et al., 2009). In view of these findings, we set out to examine the Sox6 expression pattern in the GPe (Fig. 1*g*). Sox6 immunolabeling revealed ~65% (64 ± 4%, $n = 4681$ neurons, 14 sections) of GPe neurons are Sox6-expressing (Sox6$^+$). We first investigated Sox6 expression in Nkx2.1$^+$ neurons; due to incompatibility of the Nkx2.1 and Sox6 antibodies, we relied on Sox6 immunolabeling in Nkx2.1-F-tdTom brain sections. We found substantial overlap between tdTomato$^+$ neurons and Sox6$^+$ neurons (68 ± 1% of Nkx2.1, $n = 681$ neurons, 3 sections; 58 ± 0% of Sox6, $n = 681$ neurons, 3 sections) (Table 3). Although both Sox6 and Nkx2.1 are expressed in ~60–65% of GPe neurons, they do not represent the same pool of neurons, as their expression overlaps differently with other GPe neuron markers (Table 3). Nearly all Npas1$^+$ neurons are Sox6$^+$ (93 ± 6%, $n = 1999$ neurons, 14 sections), whereas only half of the PV$^+$ population expresses Sox6 (53 ± 8%, $n = 1675$ neurons, 15 sections). As mentioned above, Nkx2.1$^+$ neurons account for ~32% of Npas1$^+$ neurons and ~83% of PV$^+$ neurons.

Next, we examined the relationship between the Sox6 and Lhx6 GPe neuron populations, as this may yield important insights into targeting the otherwise difficult-to-identify Lhx6$^+$-PV$^-$-Npas1$^-$ population. As we were unsuccessful in labeling endogenous Lhx6 protein with multiple Lhx6 antibodies (Santa Cruz Biotechnology SC-98607, Santa Cruz Biotechnology SC-271433, NeuroMab 73–241, and a custom antibody from Dr. John Rubenstein), we used the GFP expression in Lhx6-GFP mice as a proxy for Lhx6 expression. Overall, Lhx6$^+$ neurons represent a third of the GPe (34 ± 8%, $n = 2533$ neurons, 12 sections); ~30% of these neurons express PV (28 ± 7%, $n = 654$ neurons, 12 sections), 35% express Npas1 (35 ± 5%, $n = 818$ neurons, 12 sections), and 7% express ChAT (7 ± 1%, $n = 48$ neurons, 3 sections). These percentages confirm our previous reports (Hernández et al., 2015). To determine the relationship between Sox6 expression within the Lhx6$^+$, PV$^+$, and Npas1$^+$ populations, immunolabeling on Lhx6-GFP sections showed that Sox6 was expressed in ~75% (76 ± 7%, $n = 2346$ neurons, 15 sections) of Lhx6$^+$ neurons (Fig. 1*g*) as well as in all PV$^+$ neurons and Npas1$^+$ neurons that were Lhx6$^+$ (Fig. 2*a*). Note that similar to Lhx6, there were bright and dim populations of Sox6. We did not observe a relationship between Sox6 fluorescence levels and expression of PV and Npas1. Consistent with our previous observations (Hernández et al., 2015), we observed negligible overlap between Lhx6$^+$ and Foxp2$^+$ GPe neurons (8 of 1882 neurons, 3 sections).

Together, our data describe a Lhx6$^+$ population (~37%) that is devoid of both PV and Npas1 expression and accounts for ~13% of the entire GPe. A portion of this Lhx6$^+$-PV$^-$-Npas1$^-$ population does not express Sox6 and represents approximately a quarter of Lhx6$^+$ neurons (24 ± 6%, $n = 938$ neurons, 15 sections) or 8% of all GPe neurons, whereas the Lhx6$^+$-PV$^-$-Npas1$^-$ population that does express Sox6 accounts for only ~4% of the entire GPe. Given that 7% of Lhx6$^+$ neurons express ChAT, and we observed no overlap between ChAT and Sox6 (0 of 1674 neurons, 3 sections), we were able to pinpoint the molecular identity of the entirety of Lhx6$^+$ neurons (see footnote in Table 3). Importantly, the Lhx6$^+$-Nkx2.1$^+$ population is likely equivalent to the Lhx6$^+$-Sox6$^+$ population, as both Nkx2.1 and Sox6 overlap similarly with Lhx6$^+$ (Nkx2.1 of Lhx6, 78 ± 8%, $n = 1469$ neurons, 9 sections; Sox6 of Lhx6, 76 ± 7%, $n = 2346$ neurons, 15 sections), and the Lhx6$^+$-Nkx2.1$^+$ and Lhx6$^+$-

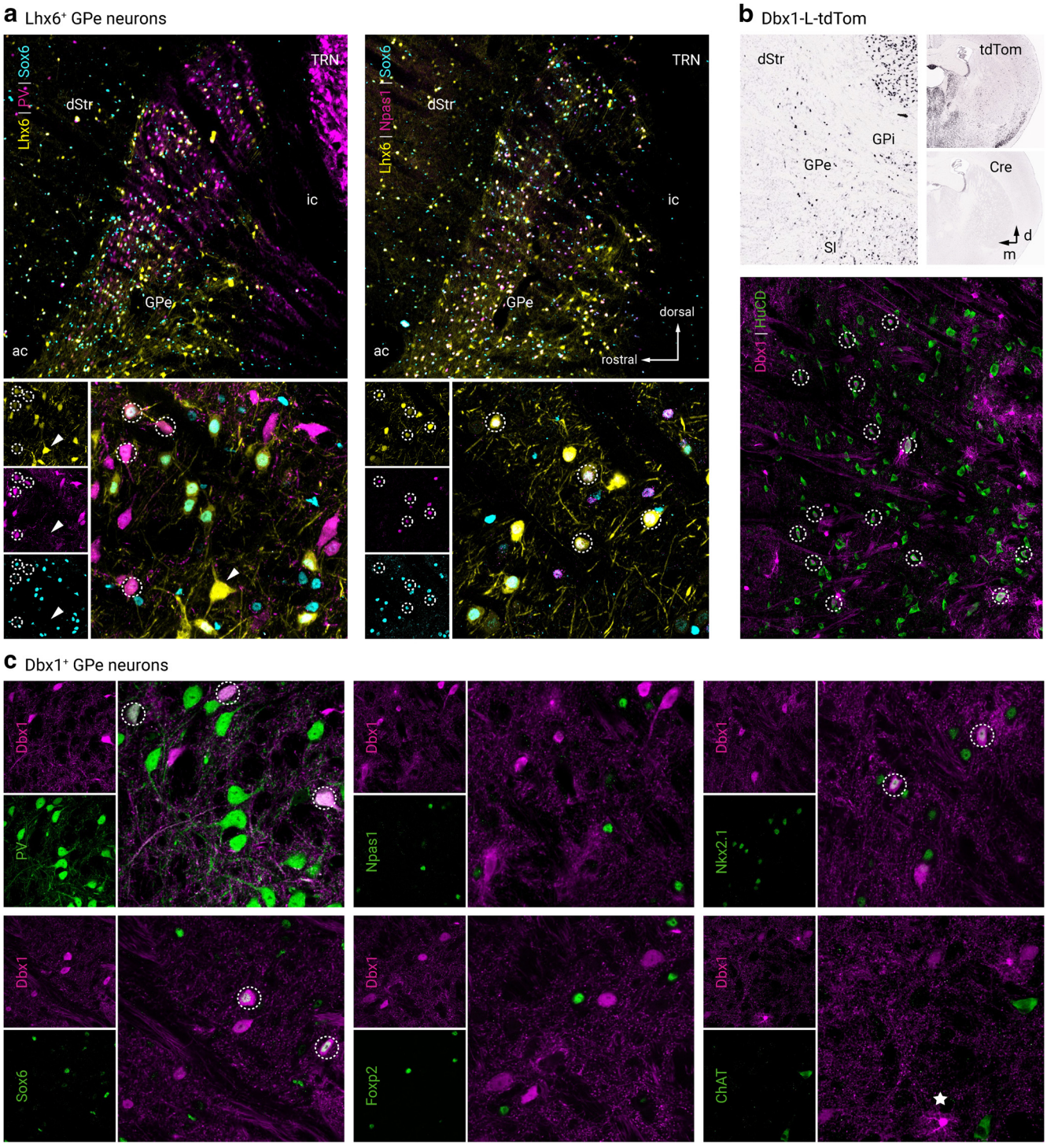

Figure 2. Lhx6^{+} and Dbx1^{+} GPe neurons colocalize with established GPe markers. ***a***, Left, low and high-magnification images of PV^{+}, Sox6^{+}, and Lhx6^{+} (GFP^{+}) GPe neurons. Right, low and high-magnification images of Npas1^{+}, Sox6^{+}, and Lhx6^{+} (GFP^{+}) GPe neurons. ***b***, *In situ* hybridization signals from Dbx1-L-tdTom mouse line for tdTomato^{+} and Cre^{+} in the adult GPe and neighboring areas (left). Note the widespread tdTomato^{+} across brain areas (top right) resulted from the cumulative recombination from early developmental stages despite the absence of Cre^{+} expression in adult (bottom right). Data are adopted from Allen Brain Atlas. The Dbx1-L-tdTom mouse line labeled Dbx1^{+} (tdTomato^{+}) neurons (HuCD, magenta) and glia in the GPe. ***c***, Dbx1^{+} GPe neurons colocalized with established GPe markers and are largely PV^{+}. Note that there was no overlap between Dbx1 and Foxp2. Circles indicate colocalization, star (bottom right) presents an example of astrocytic labeling in the Dbx1-L-tdTom mouse line. dStr, dorsal striatum; GPi, internal globus pallidus; SI, substantia innominata; TRN, thalamic reticular nucleus; ac, anterior commissure; ic, internal capsule.

Sox6^{+} populations are similarly abundant within the entire GPe (28 ± 7% and 32 ± 6%, respectively). However, with our present tools, we cannot confirm the assertion that these two subtypes are identical.

Dbx1-L-tdTom mice label a heterogenous GPe neuron subset

Since Lhx6^{+}-Sox6^{-} neurons constitute a substantial fraction (8%) of the GPe, we sought to identify an additional expression marker for this population. Neurons from the Dbx1 lineage orig-

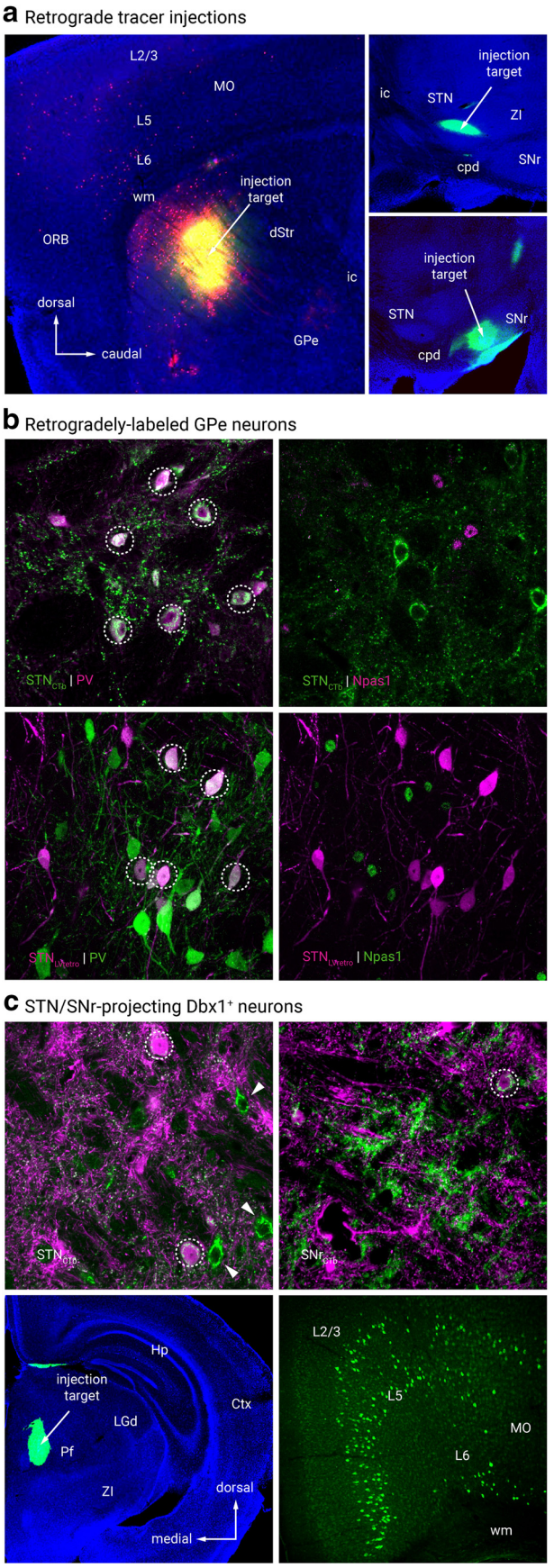

Figure 3. Retrograde tracing analysis. ***a***, Representative injection sites from retrograde tracing connectome analysis. CTb (green) with or without LVretro-Cre (LV, red) was injected into dStr (top left), STN (top right), SNr (bottom right) and mounted with DAPI (blue) to visualize cytoarchitecture. ***b***, Retrograde labeling of GPe-STN neurons with both CTb and LV tracing techniques. CTb (top left, green) labeled and LV (bottom left, magenta) GPe neurons from STN injection were primarily PV$^+$ and did not colocalize with Npas1 immunostaining (top and bottom right). ***c***, Retrograde labeling in Dbx1-L-tdTom mice shows Dbx1$^+$ neurons (magenta) project to STN (top left) and SNr (top right) as indicated by colocalization with CTb (green). Circles denote colocalization. Arrowheads denote CTb$^+$ STN projecting neurons that lack expression of Dbx1. Bottom, coronal view of a representative injection to the PF (left) along with expected positive cortical fluorescence (MO, right). No fluorescence was observed in the GPe. dStr, dorsal striatum; Ctx, cortex; GPe, external globus pallidus; GPi, internal globus pallidus; Hp, hippocampus; Pf, parafascicular nucleus; LGd, lateral geniculate, dorsal; MO, somatomotor cortex; ORB, orbital cortex; SI, substantia innominata; SNr, substantia nigra pars reticulata; STN, subthalamic nucleus; TRN, thalamic reticular nucleus; ZI, zona incerta; ac, anterior commissure; cpd, cerebral peduncle; ic, internal capsule; wm, white matter.

inate from the preoptic area (PoA) and are known to populate the GPe (Nóbrega-Pereira et al., 2010). Considering Lhx6 is expressed in postmitotic neurons derived from both the MGE and the PoA (Fogarty et al., 2007; Du et al., 2008), we set out to investigate if neurons from the Dbx1 lineage correspond to Lhx6$^+$-Sox6$^-$ GPe neurons. Accordingly, we identified neurons that arise from the Dbx1 lineage and determined their relationship with the Lhx6$^+$-Sox6$^-$ GPe subset by using a Dbx1-L-tdTom (Dbx1-Cre;LSL-tdTomato) cross, which produced robust tdTomato expression in the GPe. In addition to neuronal labeling, tdTomato$^+$ glia were present within the GPe and densely populated the ventral GPe border. For simplicity, we refer to tdTomato$^+$ neurons in Dbx1-L-tdTom mice as Dbx1$^+$ neurons. Using HuCD as a neuronal marker (Fig. 2*b*), we determined that Dbx1$^+$ neurons account for ~9% of the entire GPe population (9 ± 1%, n = 3002 neurons, 61 sections). Immunohistological analysis of Dbx1$^+$ neurons showed substantial coexpression with Nkx2.1 (78 ± 10%, n = 329 neurons, 9 sections) and Sox6 (52 ± 8%, n = 442 neurons, 15 sections). Furthermore, Dbx1$^+$ neurons are primarily PV$^+$ (72 ± 8%, n = 493 neurons, 23 sections) and to a lesser extent Npas1$^+$ (10 ± 5%, n = 72 neurons, 14 sections), ChAT$^+$ (7 ± 3%, n = 34 neurons, 9 sections), and Foxp2$^+$ (4 ± 2%, n = 13 neurons, 10 sections) (Fig. 2*c*). To summarize, we found Dbx1$^+$ neurons do not correspond to the Lhx6$^+$-Sox6$^-$ unique GPe subset. Although both populations were of similar abundance in the GPe, they varied in their coexpression of PV, Npas1, and Sox6. Expression of Lhx6 in Dbx1$^+$ neurons was not examined in this study for technical reasons; however, due to the close functional relationship between Nkx2.1, Sox6, and Lhx6, it can be inferred that Lhx6 represents a substantial fraction of Dbx1$^+$ neurons.

Dbx1$^+$-PV$^+$ neurons exhibit canonical PV$^+$ neuron projection patterns

Although Dbx1$^+$ neurons account for only ~10% of GPe neurons, it is possible that they target a unique area and serve an important function. As Cre is not expressed in adult Dbx1-Cre mice (Bielle et al., 2005) (Fig. 2*b*), we do not have true genetic access to this neuron population. Rather than relying on standard Cre-inducible viral approaches, Alexa-conjugated cholera toxin b (CTb), a widely used retrograde tracer, was used to map the axonal projection patterns of Dbx1$^+$ neurons. Given the majority of Dbx1$^+$ neurons are PV$^+$, we first targeted the STN, the principal recipient of PV$^+$ GPe input, in our connectome survey (Hernández et al., 2015; Hegeman et al., 2016). As expected, we found Dbx1$^+$ neurons project primarily to the STN (23 ± 9%, n = 94 neurons, 9 sections) (Fig. 3*c*, Table 4). Additionally, but to a much lesser extent, we found Dbx1$^+$ neurons project to the

Table 4. Quantification of retrogradely-labeled GPe neurons

	Injection targets											
	STN			SN			dStr			Ctx (ORB, MO, SS)		
	Median ± MAD	*n* (neurons)	*n* (sections)	Median ± MAD	*n* (neurons)	*n* (sections)	Median ± MAD	*n* (neurons)	*n* (sections)	Median ± MAD	*n* (neurons)	*n* (sections)
LVretro-cre												
Total tdTomato$^+$	–	750	18	–	127	12	–	406	15	–	293	24
PV$^+$	75.6 ± 6.7	278	9	66.7 ± 26.2	51	9	11.5 ± 4.8	15	6	0.0 ± 0.0	3	8
PV$^-$	20.0 ± 8.7	74	9	28.6 ± 25.3	18	9	88.5 ± 4.8	114	6	100.0 ± 0.0	62	11
Npas1$^+$	15.6 ± 6.5	45	9	15.8 ± 6.4	7	3	75.0 ± 8.3	200	9	25.0 ± 6.3	41	13
Npas1$^-$	79.1 ± 16.1	247	9	84.2 ± 6.4	51	3	25.0 ± 8.3	77	9	68.8 ± 11.3	106	13
Npas1$^+$-Nkx2.1$^+$	–	–	–	–	–	–	–	–	–	20.0 ± 6.7	8	3
Nkx2.1$^+$	–	–	–	–	–	–	–	–	–	32.3 ± 5.8	20	6
ChAT$^+$	–	–	–	–	–	–	–	–	–	50.0 ± 0.0	19	3
ChAT$^-$	–	–	–	–	–	–	–	–	–	50.0 ± 0.0	23	3
Foxp2$^+$	–	–	–	–	–	–	–	–	–	0.0 ± 0.0	0	3
CTb												
Total CTb$^+$	–	592	12	–	173	15	–	42	17	–	116	21
PV$^+$	72.6 ± 11.1	263	9	33.3 ± 11.1	14	9	0.0 ± 0.0	1	8	0.0 ± 0.0	0	3
PV$^-$	27.5 ± 10.6	99	9	66.7 ± 11.1	52	9	100.0 ± 0.0	18	8	100.0 ± 0.0	6	3
Npas1$^+$	6.4 ± 4.4	10	3	18.6 ± 8.3	19	6	100.0 ± 0.0	18	9	40.4 ± 9.7	19	6
Npas1$^-$	93.7 ± 4.4	130	3	81.4 ± 8.3	68	6	0.0 ± 0.0	5	9	60.0 ± 10.0	27	6
Dbx1$^+$	22.6 ± 9.4	94	9	2.2 ± 0.3	20	9	0.0 ± 0.0	0	17	0.0 ± 0.0	0	9
PV$^+$-Dbx1$^+$	11.8 ± 11.8	56	9	5.6 ± 5.6	10	15	0.0 ± 0.0	0	8	0.0 ± 0.0	0	3
PV$^-$-Dbx1$^+$	0.0 ± 0.0	7	9	0.0 ± 0.0	6	15	0.0 ± 0.0	0	8	0.0 ± 0.0	0	3
Npas1$^+$-Dbx1$^+$	0.0 ± 0.0	0	3	0.0 ± 0.0	2	9	0.0 ± 0.0	0	9	0.0 ± 0.0	0	6
Npas1$^-$-Dbx1$^+$	14.6 ± 2.1	27	3	0.0 ± 0.0	6	9	0.0 ± 0.0	0	9	0.0 ± 0.0	0	6

Ctx, Cortex; dStr, dorsal striatum; MAD, median absolute deviation; MO, somatomotor area; ORB, orbital area; SN, substantia nigra; SS, somatosensory area; STN, subthalamic nucleus.

substantia nigra (SN, 2 ± 0%, $n = 20$ neurons, 9 sections). These numbers are likely an underestimation due to incomplete coverage of the target areas (i.e., STN and SN) with these injections. Importantly, although ~10% of Dbx1$^+$ GPe neurons coexpress Npas1, we observed no projections to the dorsal striatum (0 of 42 CTb$^+$ neurons, 17 sections) (Table 4). The negative results were not due to poor labeling efficiency as neighboring Dbx1$^-$ neurons were evidently labeled in the same section. To examine if Dbx1$^+$ neurons account for the recently described noncholinergic, cortically-projecting GPe neurons (Van der Kooy and Kolb, 1985; Chen et al., 2015; Saunders et al., 2015; Schwarz et al., 2015; Ährlund-Richter et al., 2019; Sun et al., 2019), CTb was injected into various cortical regions of Dbx1-L-tdTom mice. Systematic analysis of multiple cortical areas including the somatomotor (MO, $n = 4$ mice), somatosensory (SS, $n = 2$ mice), anterior cingulate (AC, $n = 1$ mouse), agranular (AG) and orbital (ORB, $n = 2$ mice) cortices revealed Dbx1$^+$ neurons do not project to any of these cortical regions (0 of 52 CTb$^+$ neurons, 9 sections). The presence of CTb$^+$ neurons within the GPe confirmed that the negative results were not due to failed injections (see below).

To confirm that the findings from retrograde tracing were not just due to obscure biases with the CTb, a pseudotyped-lentivirus was used for retrograde delivery of Cre recombinase (LVretro-Cre) (Knowland et al., 2017) in LSL-tdTomato mice. Unlike CTb, this strategy gives more robust, unambiguous cytoplasmic tdTomato expression. CTb and LVretro-Cre were injected into various known areas that receive GPe input, including dStr, STN, SNr, parafascicular nucleus (PF) (Kita, 2007). We observed comparable labeling patterns with LVretro-Cre and CTb injections into the dStr (Npas1$^+_{\text{LVretro}}$: 75 ± 8%, $n = 200$ neurons, 9 sections; Npas1$^+_{\text{CTb}}$: 100 ± 0%, $n = 18$ neurons, 9 sections) and STN (PV$^+_{\text{LVretro}}$: 76 ± 7%, $n = 278$ neurons, 9 sections; PV$^+_{\text{CTb}}$: 73 ± 11%, $n = 263$ neurons, 9 sections). A different scenario was observed with SNr injections—there was not a predominant neuron class that projected to the SNr (PV$^+_{\text{LVretro}}$: 67 ± 26%, $n = 51$ neurons, 9 sections; PV$^+_{\text{CTb}}$: 33 ± 11%, $n = 14$ neurons, 9 sections) (Fig. 3*c*, Table 4). Such a discrepancy between LVretro-Cre and CTb observed in the SNr data could be attributed to a number of factors including complex topographical organization of the GPe projection and CTb spreading into areas that are adjacent to the SNr and receive Npas1$^+$ input (e.g., substantia nigra pars compacta). Furthermore, LVretro-Cre and CTb injections into the PF yielded labeling throughout the cortex, most prominently in the MO and AG regions (Fig. 3*c*), consistent with prior observations (Sherman, 2016; Mandelbaum et al., 2019). However, contrary to reports of a GPe-PF connection from other laboratories (Mastro et al., 2014), we observed no labeling in the GPe with these injections (LVretro-Cre, 4 mice; CTb, 9 mice). It is possible that CTb and LVretro-Cre both have low labeling efficiencies, making it difficult to conclude the absence of sparse projections.

Cortex and GPe are reciprocally connected

Although we found no Dbx1$^+$ neurons projecting to the cortex, we identified a subset of GPe neurons that are cortex-projecting. CTb-based tracing revealed primary somatosensory (SSp, aka S1), primary somatomotor (MOp, aka M1), AG and ORB cortices as the primary targets of cortical-projecting GPe neurons (CTb, $n = 116$ neurons, 21 sections). To confirm these regions as the primary targets, we injected LVretro-Cre into frontal cortical regions of LSL-tdTomato mice. As expected, we observed a population of retrogradely labeled GPe neurons, i.e., tdTomato$^+$ (LV, $n = 293$ neurons, 24 sections) (Fig. 4*b*).

Though cortical input is known to reach the GPe through the cortico-dStr-GPe and the cortico-STN-GPe pathways (Nambu et al., 2000; Kita, 2007; Jaeger and Kita, 2011; Iwamuro et al., 2017), there is increasing evidence that cortical input targets the GPe

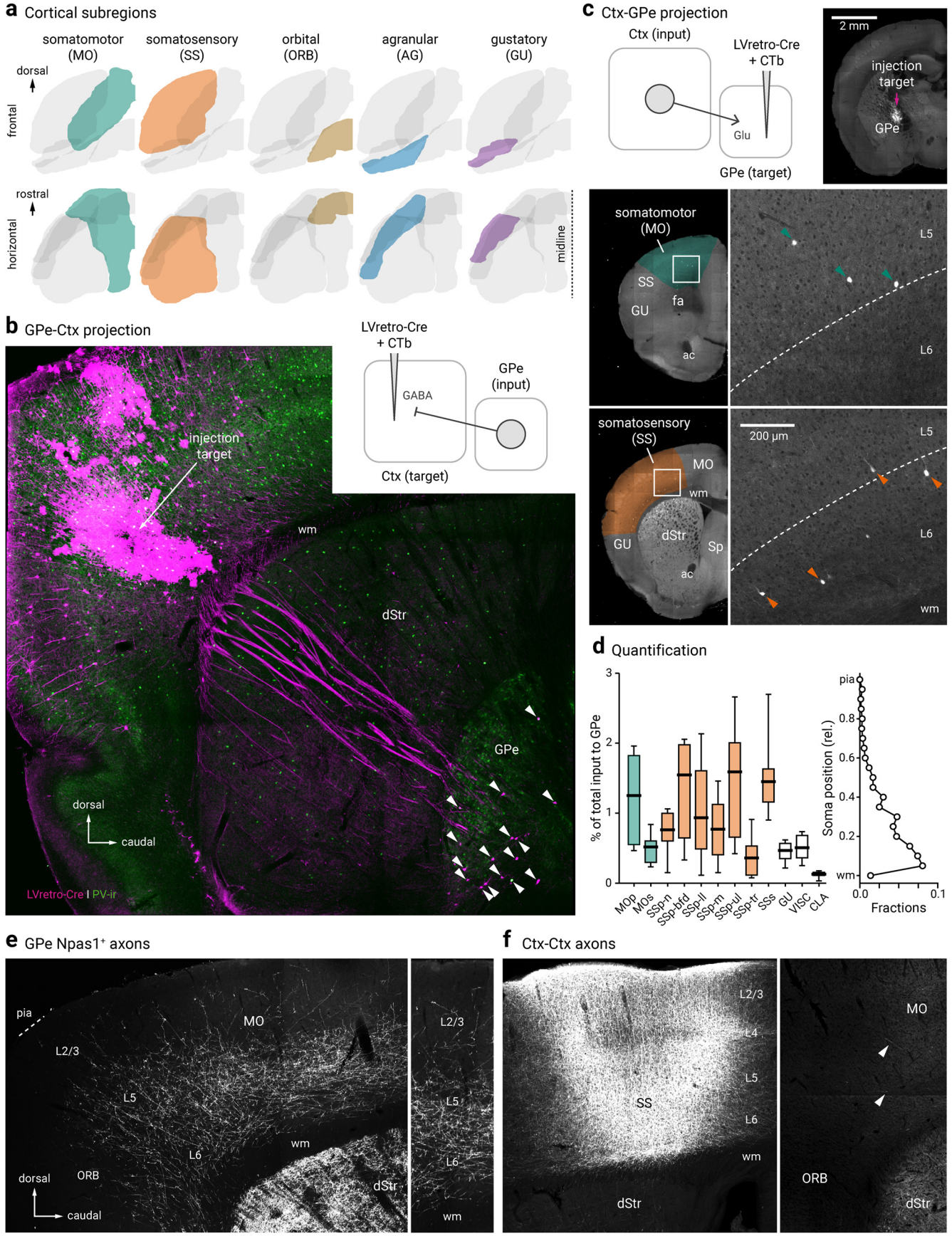

Figure 4. Cortico-pallido-cortical macroscopic anatomy. ***a***, Different cortical subregions examined in this study are highlighted. For clarity, frontal (top) and horizontal (bottom) views are shown. ***b***, A confocal micrograph showing a representative example of retrogradely-labeled cortex-projecting GPe neurons (arrowhead) using LVretro-Cre in a LSL-tdTomato mouse; PV-immunolabeling (green) was performed in this example. Inset: experimental setup. LVretro-Cre and CTb were injected into different cortical areas mentioned in ***a***, ***c***, Top left, (*Figure legend continues.*)

directly (Naito and Kita, 1994; Milardi et al., 2015; Smith and Wichmann, 2015; Karube et al., 2019). Using rabies virus tracing, we have recently confirmed the existence of cortical input to GPe neurons (Jeong et al., 2016; Hunt et al., 2018). However, we have not provided a complete representation of the input regions and their relative size. In this study, we sought to map the input from the entire cortical mantle with LVretro-Cre in LSL-tdTomato mice. Automated, serial two-photon tomography was used to provide an unbiased quantification and atlas registration (see Materials and Methods). As expected, input neurons (i.e., tdTomato$^+$) from a wide array of brain regions to the GPe were evident (data not shown). A full description of the brain-wide input to the GPe will be detailed in a later publication. The cortical input amounts to ~10% of the total input to the GPe ($n = 4205$ of 45223 neurons, 8 mice). Consistent with our previous observation, a notable input comes from the SSp followed by MOp. Additionally, but to a much lesser extent, input cells were found primarily in layers 5 and 6 of MOs, SSs, and lateral regions, such as gustatory area, visceral area, and claustrum. These results are summarized in Figure 4, *c* and *d*.

Npas1$^+$-Nkx2.1$^+$ neurons are cortex-projecting

A substantial amount of the cortex-projecting neurons displayed a distinctive larger soma and were located in the caudoventral regions of the GPe—features that are characteristic of ChAT$^+$ neurons (Fig. 5*a*). Immunolabeling for ChAT revealed 50% (50 ± 0%, $n = 19$ of 42 neurons, 3 sections) of tdTomato$^+$ neurons were ChAT$^+$. The remaining cortex-projecting GPe neurons were ChAT$^-$, i.e., noncholinergic. Our results are highly consistent with prior observations (Saunders et al., 2015; Ährlund-Richter et al., 2019). However, as the identity of noncholinergic, cortically projecting neurons remains elusive, we sought to characterize the molecular profile of these neurons. Through immunolabeling, we identified the ChAT$^-$ neurons to be Nkx2.1$^+$ (32 ± 6%, $n = 20$ of 68 neurons, 6 sections) and Npas1$^+$ (25 ± 6%, $n = 41$ of 147 neurons, 13 sections). Furthermore, a population of cortex-projecting neurons was found to be both Nkx2.1$^+$ and Npas1$^+$ (20 ± 7%, $n = 8$ of 36 neurons, 3 sections) (Table 4). As expected, the same neurons that expressed Npas1 and Nkx2.1 did not express Foxp2 (0 of 36 neurons, 3 sections). Similarly, we observed a very small fraction of neurons that were immunoreactive for PV (0 ± 0%, $n = 3$ of 65 neurons, 8 sections). Although abundant retrogradely-labeled neurons were found with injections targeting MOp, SSp, AG and ORB, we observed low levels or nondetectable retrograde labeling with injection to neighboring frontal regions such as secondary somatomotor (MOs, aka M2) and secondary somatosensory (SSs, aka S2) cortices.

To further demonstrate that Npas1$^+$ neurons project to the cortex, we injected Npas1-Cre-tdTom mice with a Cre-inducible ChR2-eYFP AAV (see Materials and Methods) into the GPe to trace the arborization patterns of Npas1$^+$ axons. Consistent with our previous studies (Hernández et al., 2015; Glajch et al., 2016), dense Npas1$^+$ axons were visible in the dStr. Moreover, we observed axons throughout the MO and SS, but its density dropped off precipitously once passed the ORB. This axonal projection pattern is distinct from that of ChAT$^+$ neurons, which arborizes more broadly, including in more caudal regions of the cortex (Parent et al., 1981; Moriizumi and Hattori, 1992; Saunders et al., 2015). To confirm axons observed in the frontal cortex were not a result of ectopic infection of caudal cortical regions, we injected the same Cre-inducible ChR2-eYFP AAV into the SSp region directly above the GPe. We observed only sparse cortico-cortical axons running rostrocaudally (Fig. 4*f*), further confirming that the axons observed in the frontal regions were indeed projections from Npas1$^+$ neurons.

The Npas1$^+$ axons appeared to arborize heavily in layers 5 and 6 and were present as superficial as layer 2/3 (Fig. 4*e*). Under high magnification, perisomatic basket-like structures can be found in layer 5 of the MO. In addition, Npas1$^+$ axons were found in the TRN, with more moderate projections in the zona incerta (ZI) and SN. Within the SN, we observed a higher density of fibers in the SNc (data not shown). The presence of Npas1$^+$ axons in the TRN is consistent with the high density of Nkx2.1$^+$ synaptic boutons in the area (Fig. 5*c*). As TRN neurons do not express Nkx2.1, the synaptic boutons observed arose from an extrinsic source. These observations suggest Npas1$^+$-Nkx2.1$^+$ GPe neurons form this projection, and thus provide new insights into the molecular identity of GPe neurons that project to the TRN (Asanuma, 1989, 1994; Cornwall et al., 1990; Hazrati and Parent, 1991; Gandia et al., 1993; Shammah-Lagnado et al., 1996; Kayahara and Nakano, 1998; Pazo et al., 2013; Clemente-Perez et al., 2017; Nakajima et al., 2019).

To evaluate the contact probability and the physiological properties of the synaptic connections from Npas1$^+$-Nkx2.1$^+$ neurons to the cortex and TRN, Npas1$^+$ neurons in the GPe were infected with a ChR2-eYFP AAV; optogenetic-based mapping and patch-clamp recordings were performed from unidentified neurons in the cortex and TRN. As Npas1 axons primarily arborized in cortical layers 5 and 6, neurons in these layers were targeted for recording. In 3 of 37 cortical neurons recorded, large (438.5–821.7 pA, $n = 3$ neurons) IPSCs (IPSCs) were evoked by optogenetic activation of Npas1$^+$ axons from the GPe (see Materials and Methods). These were not conducting events, as they were not abolished by the co-application of tetrodotoxin (1 μM) and 4-aminopyridine (100 μM). To confirm the GABAergic nature of the events, SR95531 (a $GABA_A$ receptor antagonist, 10 μM) was applied, which completely abolished evoked IPSCs (Fig. 5*d*). In contrast to the apparent low connection probability in the cortex, large IPSCs were readily evoked optogenetically in all but one of the TRN neurons tested (707.8 ± 383.8 pA, $n = 5$ neurons) (Fig. 5*f*). Importantly, as identical optogenetic conditions were used for both experiments, these data argue that the low connection probability detected in the cortex is reflective of selective targeting of cortical neuron subtypes by Npas1$^+$ axons. No photocurrents

←

(*Figure legend continued.*) experimental setup: LVretro-Cre and CTb were injected into the GPe. Cortical inputs to the GPe were mapped using two-photon tomography. Top right, Two-photon image showing the location of the injection site. Bottom, representative two-photon images from coronal sections showing GPe-projecting cortical neurons were found primarily in layer 5 and 6 of MO and SS. ***d***, Left, quantification of GPe-projecting neurons across the entire cortex. Medians, interquartile ranges, and 10th to 90th percentiles are represented in a graphical format. Right, laminar position of GPe-projecting neurons. ***e***, Low-magnification image of Npas1$^+$ pallido-cortical axons spanning across ORB, MO, and SS. Note the highest density occurred in layers 5 and 6 of MO followed by SS and dropped off precipitately rostrally in the ORB. Axons extend as far as layer 2/3. ***f***, Local cortical infection in a Npas1-Cre-tdTom mouse confirmed axons visible in rostral cortical regions were from GPe projection and not ectopic infection of cortical neurons in the caudal areas. Injection site in SS (left) resulted in very low density of caudal to rostral cortico-cortical connectivity in MO and ORB (right). Arrowheads indicate the presence of cortical axons that arose from the more caudal regions. dStr, dorsal striatum; CLA, claustrum; MOp, primary somatomotor; MOs, secondary somatomotor; ORB, orbital; Sp, septum; SSp-*n*, primary somatosensory, nose; SSp-bfd, primary somatosensory, barrel field; SSp-ll, primary somatosensory, lower limb; SSp-m, primary somatosensory, mouth; SSp-ul, primary somatosensory, upper limb; SSp-tr, primary somatosensory, trunk; SSs, secondary somatosensory; VISC, visceral; ac, anterior commissure; fa, anterior forceps; wm, white matter.

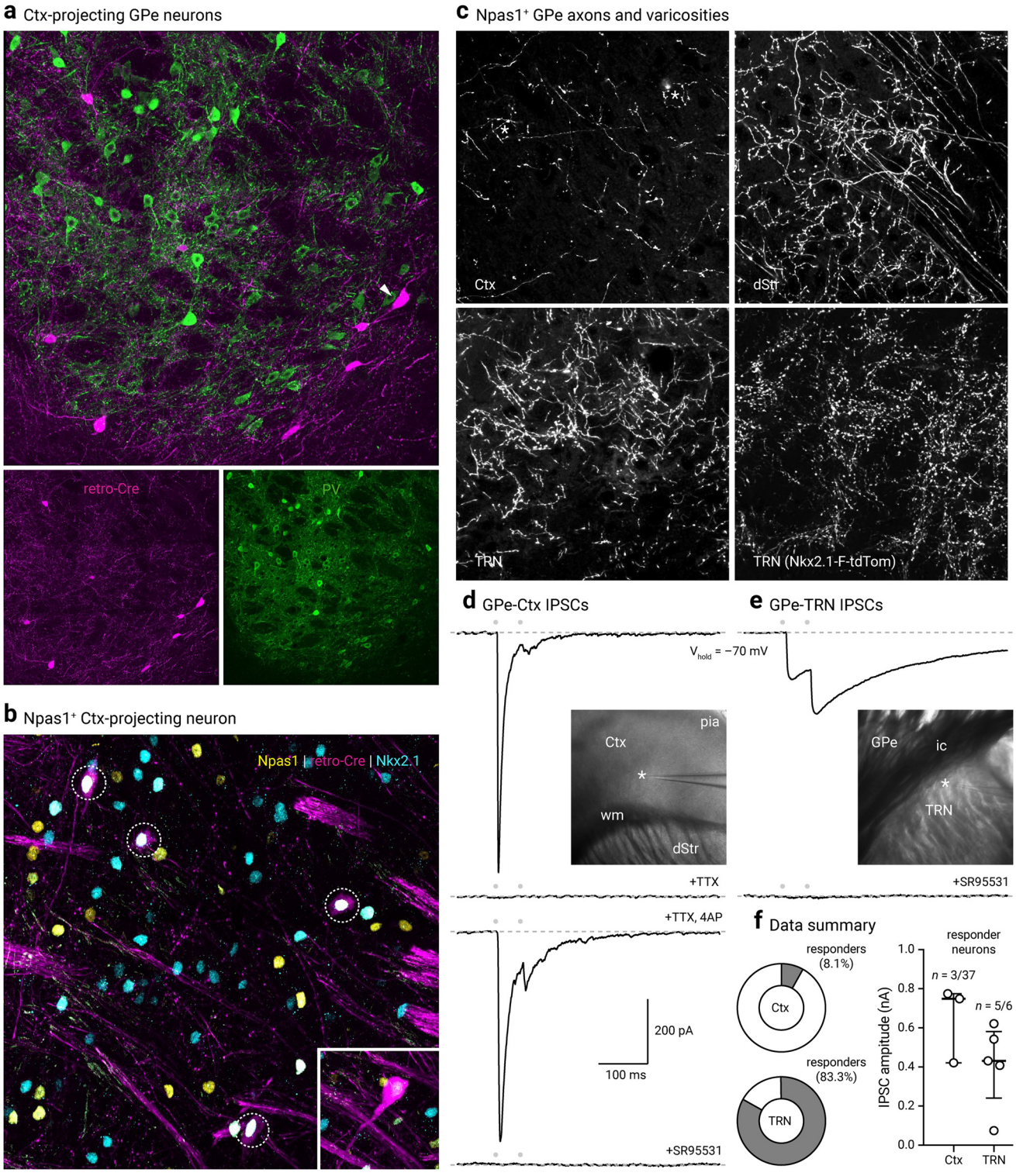

Figure 5. Cortex-projecting neuron properties. ***a***, LV retrograde labeled (magenta) GPe neurons with PV immunostaining (green). Note that cortical projecting GPe neurons are not PV^{+}. Arrowhead indicates a LV-labeled neuron with a large cell body characteristic of cholinergic neurons. ***b***, Confocal micrograph showing the coexpression (dotted circles) of Npas1 (yellow) and Nkx2.1 (blue) in cortex-projecting GPe neurons (magenta). Inset: an example of a neuron (shown at the same magnification) that has a large cell body and low Nkx2.1 expression, features of cholinergic neurons within the confines of the GPe. ***c***, High-magnification confocal micrographs of axons in the Ctx, dStr, and TRN with injection of a CreOn-ChR2 AAV into the GPe of a Npas1-Cre-tdTom mouse. Asterisks in the top left denote putative terminals. Bottom right, high density of synaptic boutons in the TRN of Nkx2.1-F-tdTom mice. ***d***, Voltage-clamp recordings of the Npas1^{+} input in a cortical neuron within layers 5 and 6. The recorded neuron was held at -70 mV with a high Cl^{-} internal; IPSCs (IPSCs) were evoked from 20 Hz paired-pulse blue light stimulation (indicated by gray circles). Note the fast and depressing responses evoked. Inset: location of the recorded neuron (asterisk) in the Ctx is shown. IPSCs were attenuated with extracortical stimulation (data not shown) and abolished with tetrodotoxin (TTX, 1 μM). Application of 4-aminopyridine (4-AP, 100 μM) in the presence of TTX restored the response with intracortical stimulation. IPSCs were completely blocked with SR95531 (10 μM). ***e***, Voltage-clamp recording of a TRN neuron with identical experimental setup shown in ***d***, Note the facilitating responses evoked. Inset: location of the recorded neuron (asterisk) is shown. Responses were sensitive to the application of SR95531 (10 μM). ***f***, Left, Pie charts summarizing the percentages of responders in Ctx and TRN. Right, Medians and interquartile ranges of IPSC amplitudes are represented in a graphical format. dStr, dorsal striatum; Ctx, cortex; TRN, thalamic reticular nucleus; ic, internal capsule; wm, white matter.

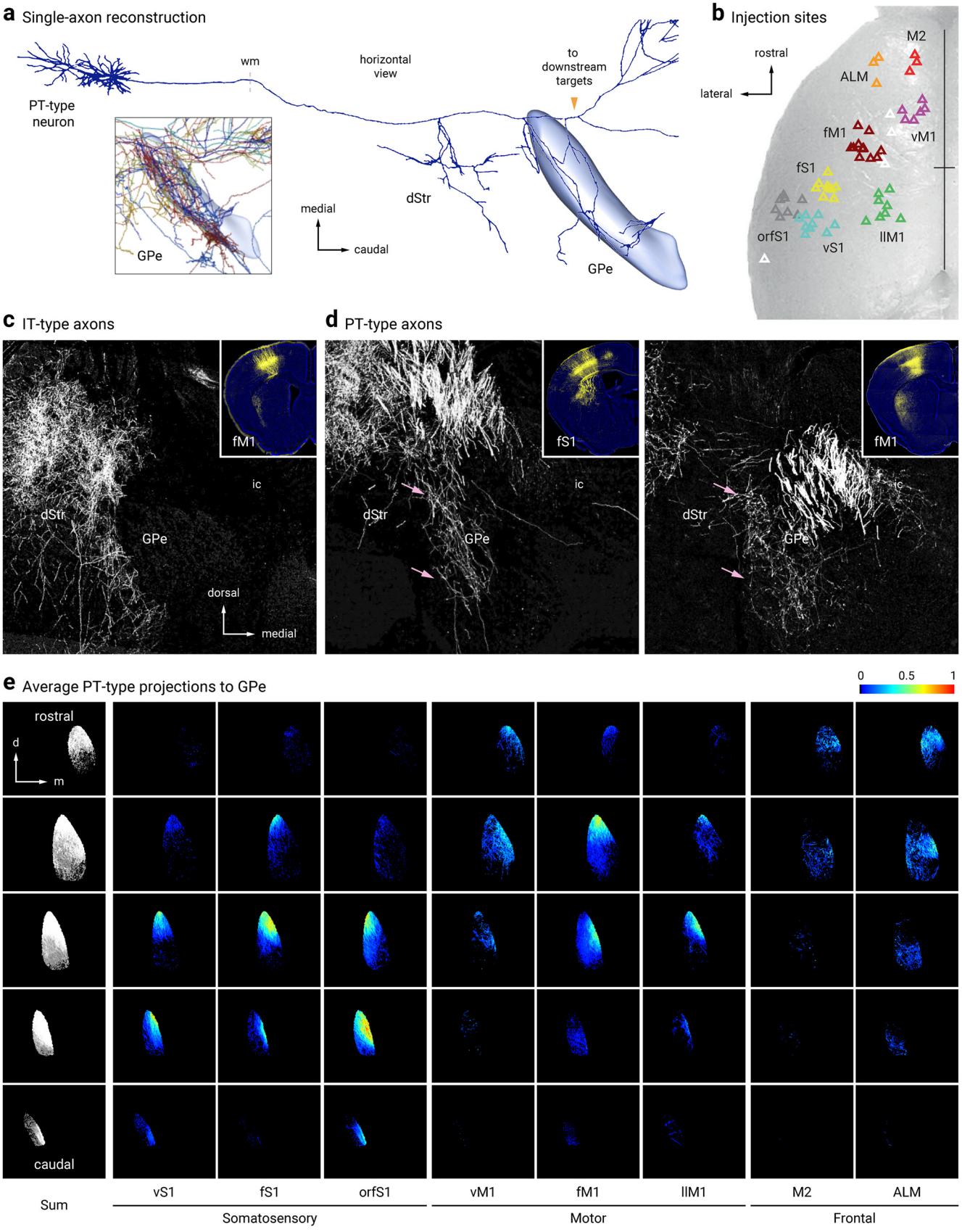

Figure 6. Pyramidal-tract but not intratelencephalic axons collateralize in the GPe. ***a***, Single-axon reconstruction of a layer 5 (L5) cortico-pallidal neuron (neuron #AA0122) in the motor cortex. Data are adapted from the MouseLight project (http://mouselight.janelia.org). The axonal projection pattern is consistent with a pyramidal-tract (PT)-type neuron. Inset: axonal arborization of 10 different cortical neurons. GPe and axonal endpoint were used as the target location and structure queries, respectively. ***b***, Injection site center of mass of Sim1-Cre (L5-PT) plotted and spatially clustered ($n = 62$, triangles). These injection sites correspond to vibrissal, forelimb, and orofacial somatosensory cortices (vS1, fS1, and orfS1); vibrissal, forelimb, (*Figure legend continues.*)

were observed in any of the recorded neurons, ruling out potential contributions of the synaptic events from ectopic infection of neurons local to the recorded areas.

Pyramidal tract-type cortical neurons target the GPe

Consistent with our two-photon tomography analysis (Fig. 4*c*,*d*), single-axon reconstruction data from the MouseLight project (Economo et al., 2016) suggest that GPe-projecting cortical neurons are predominantly pyramidal tract (PT)-type. They are thick tufted pyramidal neurons that are located in the lower layer 5 (L5B), do not have cross-hemispheric collaterals, and are multiprojectional (Kita and Kita, 2012; Harris and Shepherd, 2015; Kawaguchi, 2017; Hooks et al., 2018; Shibata et al., 2018) (Fig. 6*a*). This inference corroborated the anterograde viral-tracing data derived from a Sim1-Cre (PT-specific driver line) (Gerfen et al., 2013)—both single-axon (Fig. 6*a*) and bulk tracing data argue that cortical axons enter the GPe (Fig. 6*d*,*e*). In contrast, similar experiments with Tlx3-Cre (an intratelencephalic-specific driver line) suggest that intratelencephalic neurons do not provide input to the GPe (Fig. 6*c*). Overall, there were general similarities between the topographical organization of the cortico-striatal projections and the cortico-pallidal projections; both frontal and motor projections targeted more rostral areas of the GPe, whereas sensory projections targeted more posterior ones (Hintiryan et al., 2016; Hooks et al., 2018).

To provide a confirmation of the existence of synaptic terminals formed by cortical axons in the GPe, we injected AAVretro-ChR2-eYFP into the GPe of Emx1-Cre mice (Gorski et al., 2002). This resulted in selective ChR2-eYFP expression in cortical neurons and their axons in the GPe, STN, and dStr (Fig. 7*a*). A high density of labeled neurons (and processes) were observed within the ORB, MO, and SS. This expression pattern is in agreement with our two-photon tomography data (Fig. 4*c*,*d*) and the axonal projection patterns revealed by Sim1-Cre (Fig. 6*d*,*e*). Furthermore, these data reinforce the idea that the cortical axons observed in the GPe in both the single axon and bulk tracking studies were not simply passage fibers. Consistent with this idea, colocalization of VGluT1 in ChR2-eYFP-labeled varicosities was readily observed (Fig. 7*b*). To provide more definitive evidence, *ex vivo* voltage-clamp recordings were performed; optogenetic activation of cortical input evoked EPSCs in 20 of 25 GPe neurons. However, the size of the EPSCs (29.0 ± 18.2 pA) spans over three orders of magnitude in the recorded neurons. Consistent with the single-axon and bulk tracing data, which both show that cortico-pallidal neurons produce collaterals within the dStr, EPSCs (100.8 ± 79.1 pA) were evoked readily across all striatal projection neurons tested ($n = 6$) (Fig. 7*d*).

Lhx6$^+$ neuron subtypes have unique spatial patterns

Spatial distribution may vary with neuronal identity, as seen in the cortex, for example, where neurons are organized in a highly laminar-specific manner (Huang et al., 2007; Harris and Shepherd, 2015; Wamsley and Fishell, 2017). We therefore integrated spatial distribution as a metric to phenotype different GPe neuron types (Figs. 8, 9). Overall, more neurons populate toward the rostral pole of the GPe. We noted that ChAT$^+$ neurons and Lhx6$^+$-Sox6$^+$ neurons are displaced more heavily toward the caudoventral regions and rostroventral regions, respectively. All other identified neurons are more evenly distributed throughout the GPe. This analysis, however, does not capture any lateromedial gradients. As neurons were routinely sampled from three different lateromedial planes across the GPe, the abundance of identified neurons were tallied. Consistent with previous studies (Mastro et al., 2014; Hernández et al., 2015), we observed a lateromedial gradient of PV$^+$ neurons (lateral = 46 ± 10%, n = 4368 neurons, 24 sections; intermediate = 45 ± 11%, n = 5113 neurons, 27 sections; medial = 32 ± 7%, n = 2829 neurons, 20 sections) and Lhx6$^+$ neurons (lateral = 28 ± 6%, n = 1422 neurons, 10 sections; intermediate = 42 ± 9%, n = 2050 neurons, 10 sections; medial = 45 ± 12%, n = 2190 neurons, 8 sections). PV$^+$ neurons were more concentrated in the lateral than the medial level; the reverse pattern was found for Lhx6$^+$ neurons. In Figure 9, we illustrate the distribution of Lhx6$^+$-Sox6$^-$ neurons (lateral = 8 ± 4%, n = 187 neurons, 5 sections; intermediate = 10 ± 1%, n = 292 neurons, 5 sections; medial = 21 ± 7%, n = 459 neurons, 5 sections), which follow the same pattern as pan-Lhx6$^+$ neurons. Although PV$^+$-Lhx6$^+$ neurons displayed a similar pattern (lateral = 8 ± 2%, n = 116 neurons, 4 sections; intermediate = 11 ± 6%, n = 202 neurons, 3 sections; medial = 8 ± 1%, n = 175 neurons, 3 sections) as pan-Lhx6$^+$ neurons, Npas1$^+$-Lhx6$^+$ neurons do not (lateral = 14 ± 2%, n = 231 neurons, 4 sections; intermediate = 15 ± 2%, n = 308 neurons, 4 sections; medial = 14 ± 2%, n = 284 neurons, 4 sections). The lateromedial gradients of different GPe neuron types are summarized in Figure 9.

GPe neuron subtypes have distinct intrinsic properties

To further define GPe neuron subtypes, *ex vivo* electrophysiological analyses were performed systematically on genetically-identified GPe neuron subtypes, including the less well studied neuron subtypes. We used recording and analysis routines (see Materials and Methods) identical to those used in our previous study to facilitate cross-comparison between the two (Hernández et al., 2015).

To identify Foxp2$^+$ neurons, we infected Foxp2-Cre mice in the GPe with a CreOn-mCherry AAV (see Materials and Methods). To confirm the validity of the approach, a subset of these mice were examined for cellular specificity of Cre-mediated mCherry expression (mCherry$^+$). In nearly all mCherry$^+$ neurons examined, Foxp2 was expressed (100 ± 0%, n = 473 of 485 neurons, 6 sections). No GPe neurons expressed mCherry when the same virus was injected in wild-type mice (n = 2 mice, 6 sections). For electrophysiological analysis, we qualitatively categorized Lhx6$^+$ neurons as "bright" and "dim" based on their GFP expression level (Fig. 10*a*), though the definitive identities of Lhx6$^+_{\text{bright}}$ and Lhx6$^+_{\text{dim}}$ neurons were not confirmed *post hoc*. To identify PV$^+$-Dbx1$^+$ neurons, an intersectional cross was made—PV-Dbx1-FL-tdTom (PV-Flp;Dbx1-Cre;LSL-FSF-tdTomato)—to label PV$^+$-Dbx1$^+$ neurons (tdTomato$^+$) (Fig. 10*a*). To unequivocally identify Npas1$^+$-Lhx6$^+$ neurons, which are equivalent to Npas1$^+$-Nkx2.1$^+$ neurons, we crossed Npas1-tdTom and Lhx6-GFP mice. Double-positive (tdTomato$^+$ and

←

(*Figure legend continued*.) and lower limb motor cortices (vM1, fM1, and lIM1); and frontal areas (anterior lateral motor cortex (ALM) and secondary motor cortex (M2)). Eight clusters shown in red (M2), orange (ALM), purple (vM1), burgundy (fM1), green (lIM1), yellow (fS1), teal (vS1), and gray (orfS1). Indeterminate injection sites are white. Sites are superimposed on an image of the dorsal surface of mouse cortex. Black cross marks indicate midline and bregma. For simplicity, injection sites in Tlx3-Cre (L5-IT) are not shown (see Hooks et al., 2018, for further information). ***c***, ***d***, Tlx3-Cre (IT-type) projections from fM1 in dStr but not GPe. Sim1-Cre (PT-type) projections from fS1 (left) and fM1 (right) in dStr and GPe (pink arrows). Inset: Coronal images of injection sites in Tlx3-Cre and Sim1-Cre showing the cell body locations and their axonal projections. ***e***, Coronal images of the average normalized PT-type projection to GPe from eight cortical areas. Each column is a cortical projection, with rows going from anterior (top) to posterior (bottom). Each projection is normalized for comparison within the projection.

GFP$^+$) neurons were targeted for recordings. ChAT$^+$ neurons, which can be identified based on their unique somatodendritic morphology, were not included in this analysis as we have previously established that they have a very distinct electrophysiological profile (Hernández et al., 2015). Last, because we do not have genetic access to Lhx6$^+$-Sox6$^-$ neurons, we did not have a means to target them for direct recording.

To highlight, Foxp2$^+$ neurons and PV$^+$-Dbx1$^+$ neurons were at the extremes in terms of their spontaneous activity level measured in cell-attached recordings (Foxp2$^+$ = 6.1 ± 1.9 Hz, n = 20; PV$^+$-Dbx1$^+$ = 18.4 ± 3.6 Hz, n = 16), with the rest of the neuron subtypes displaying properties traversing the spectrum. Furthermore, our results corroborate findings from our prior studies (Hernández et al., 2015) that PV$^+$ neurons fire at a higher rate than Npas1$^+$ neurons (PV$^+$ = 16.7 ± 3.4 Hz, n = 111; Npas1$^+$ = 8.4 ± 3.1 Hz, n = 63, p < 0.0001). Lhx6$^+$ neurons exhibited firing rates that are in between PV$^+$ neurons and Npas1$^+$ neurons (Lhx6$^+$ = 10.5 ± 5.1 Hz, n = 43). Within the Lhx6$^+$ population, Lhx6$^+_{bright}$ neurons and Lhx6$^+_{dim}$ neurons exhibited different firing rates (Lhx6$^+_{bright}$ = 8.1 ± 2.7 Hz, n = 18; Lhx6$^+_{dim}$ = 16.5 ± 1.2 Hz, n = 7, p = 0.0039). Additionally, the Npas1$^+$-Lhx6$^+$ neurons had a higher spontaneous firing than the Foxp2$^+$ population (Npas1$^+$-Lhx6$^+$ = 10.4 ± 2.8 Hz, n = 14, p = 0.021) but was comparable to Lhx6$^+_{bright}$ neurons (p = 0.17) (Fig. 10*b*). As expected, Dbx1$^+$ neurons exhibited firing behavior that was most consistent with its composition, with most neurons exhibiting similar firing rates to PV$^+$ neurons and some more similar to Npas1$^+$ neurons (Tables 5, 6, Dbx1$^+$ = 13.2 ± 2.7 Hz, n = 21).

As we have previously shown that the regularity of the firing varied with GPe neuron types (Hernández et al., 2015), we measured the coefficient of variation in the interspike-interval (CV_{ISI}). Consistent with our prior observations, PV$^+$ neurons exhibited a lower CV_{ISI} than Npas1$^+$ neurons (PV$^+$ = 0.14 ± 0.03, n = 111; Npas1$^+$ = 0.27 ± 0.10, n = 63, p < 0.0001). Dbx1$^+$ neurons and PV$^+$-Dbx1$^+$ neurons had CV_{ISI} that were statistically similar to those of PV$^+$ neurons (Dbx1$^+$ = 0.14 ± 0.03, n = 21; PV$^+$-Dbx1$^+$ = 0.16 ± 0.05, n = 16). Foxp2$^+$ neurons had the largest variability in their firing rate, as indicated by the highest CV_{ISI} within the GPe neuronal population (Foxp2$^+$ = 0.36 ± 0.09, n = 20). Npas1$^+$-Lhx6$^+$ neurons had CV_{ISI} statistically similar to that of the Lhx6$^+_{bright}$ neurons (Npas1$^+$-Lhx6$^+$ = 0.25 ± 0.07, n = 14, Lhx6$^+_{bright}$ = 0.21 ± 0.04 n = 18, p = 0.51).

To provide comprehensive electrophysiological profiles, we investigated a range of electrophysiological properties of GPe neurons in whole-cell current-clamp recordings. As seen in prior

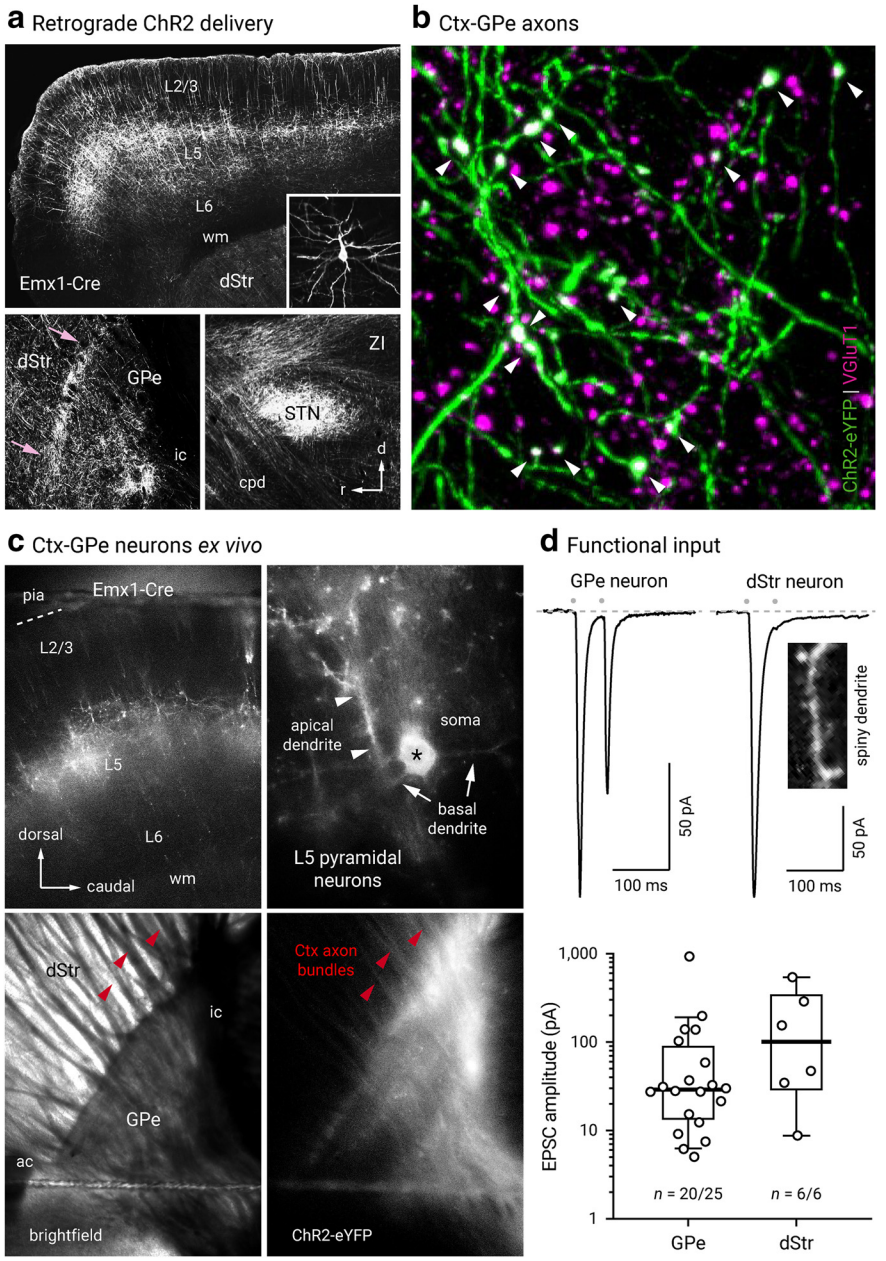

Figure 7. Cortex neurons form functional synapses on GPe neurons. ***a***, Top, Confocal micrograph of a sagittal section from an Emx1-Cre mouse, showing the neuronal elements expressing ChR2-eYFP delivered from an AAVretro injection into the GPe. Inset, ChR2-eYFP$^+$ layer 5 neuron with morphology typical of pyramidal neurons is shown. Bottom left, Cortical axons were observed at the GPe level. An enrichment of axons was present at the rostral pole of the GPe, immediate adjacent to the dStr (pink arrows). Bottom right, High density of cortico-pallidal axons were observed to collateralize in the subthalamic nucleus (STN). ***b***, A high-magnification image showing the colocalization (white arrowheads) of VGluT1 (magenta) in corticopallidal axons (green). ***c***, Epifluorescence image from *ex vivo* tissue showing robust expression of ChR2-eYFP in cortical neurons. Top, AAVretro-CreOn-ChR2-eYFP was injected into the GPe of an Emx1-Cre mouse. Robust ChR2-eYFP expression in the MO was observed (left). ChR2-eYFP$^+$ neurons were readily seen at high-magnification (right). Asterisk indicates the soma of a typical ChR2-eYFP$^+$ neuron. Bottom, Cortico-pallidal axons were preserved in an *ex vivo* slice preparation. ***d***, Top, Functional cortical inputs were recorded in GPe neurons (20 of 25) and dStr projection neurons (6 of 6). EPSCs were evoked with optogenetics. Bottom, Box and scatter plots summarizing EPSC amplitude recorded from GPe neurons (left) and dStr SPNs (right). Note the large variance in the data. Red arrowheads indicate cortical axon bundles; white arrowheads indicate apical dendrites. dStr, dorsal striatum; GPe, external globus pallidus; STN, subthalamic nucleus; ZI, zona incerta; ac, anterior commissure; cpd, cerebral peduncle; ic, internal capsule; wm, white matter.

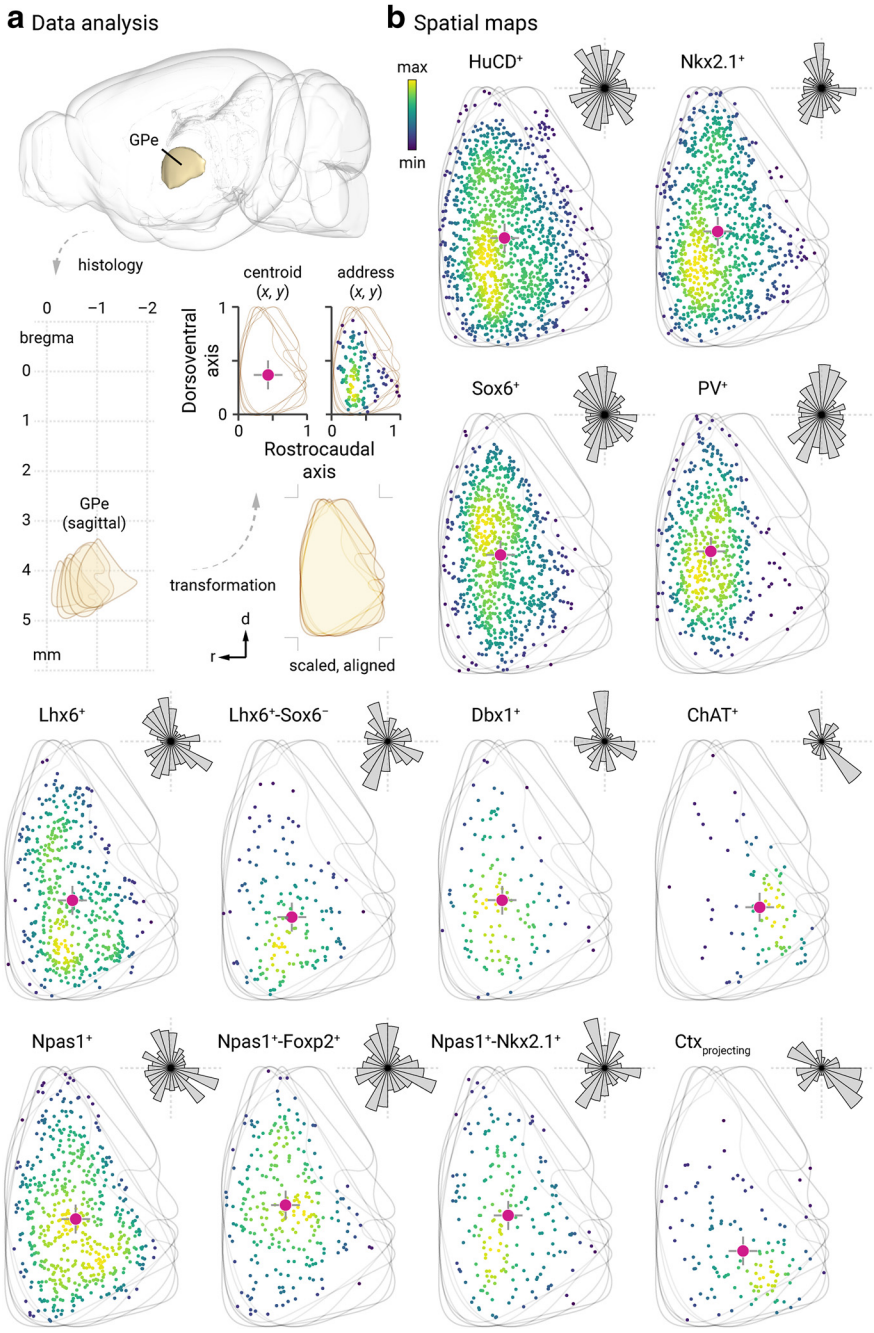

Figure 8. Spatial distribution of GPe neuron subtypes. ***a***, Spatial information of GPe neurons cannot be represented relative to bregma location (top, lower left) because of its complex geometry. To mathematically describe the spatial distribution of GPe neurons in each brain section, fixed mouse brains were sagittally sectioned and histologically processed. Images were manually aligned to a reference atlas. GPe neurons located at six different lateromedial levels (2.73 mm, 2.53 mm, 2.35 mm, 2.15 mm, 1.95 mm, and 1.73 mm) were charted and collapsed onto a single plane. As the GPe is similarly shaped across the lateromedial extent (lower right), both the rostrocaudal and dorsoventral extent were assigned to 0 and 1. The address of each neuron is defined by their *x*–*y* coordinates and represented with a marker (black). To capture the aggregate spatial distribution, a geometric centroid (red) of each neuron population was then determined to represent the center of mass in both *x* and *y* dimensions. Centroids are then used as the origin for the polar histograms in ***b***, Size of each sector represents the relative neuron count as a function of direction. ***b***, Representative data of neurons from two individual mice are shown in each case, except for retrogradely labeled cortically projecting neurons (*n*, 7 mice; 119 neurons; 15 sections). Each marker represents a neuron. The density of neurons are encoded with a yellow-blue gradient. Hash marks, which represent the dorsoventral and rostrocaudal axes, are presented with the centroids and polar histograms to facilitate comparison. Bin sizes in the polar histograms were chosen based on the size of each neuron population. The (*x*, *y*) centroid values for the respective GPe distributions were as follows: HuCD$^+$ (0.3798, 0.4168); Nkx2.1$^+$ (0.3599, 0.4439); Sox6$^+$ (0.3587, 0.4529); PV$^+$ (0.3205, 0.4699); Lhx6$^+$ (0.3918, 0.3827); Lhx6$^+$-Sox6$^-$ (0.3755, 0.3164), Dbx1$^+$ (0.3679, 0.3828); ChAT$^+$ (0.6024, 0.3569); Npas1$^+$ (0.4106, 0.4140); Npas1$^+$-Foxp2$^+$ (0.3695, 0.4676); Npas1$^+$-Nkx2.1$^+$ (0.4026, 0.4278); Ctx-projecting GPe neurons (0.5061, 0.2911).

studies, PV$^+$ neurons had the highest maximum firing rate (PV$^+$ = 198 ± 24 Hz, n = 49). Lower maximum firing rates were observed in Npas1$^+$ neurons and Foxp2$^+$ neurons (Npas1$^+$ = 96 ± 34 Hz, n = 33; Foxp2$^+$ = 55 ± 23, n = 16) when compared with PV$^+$, Dbx1$^+$, and PV$^+$-Dbx1$^+$ neurons ($p < 0.0001$ for all). Within the Lhx6 population, Lhx6$^+_{bright}$ neurons and Lhx6$^+_{dim}$ neurons exhibited different maximum firing rates (Lhx6$^+_{bright}$ = 93 ± 31 Hz, n = 24; Lhx6$^+_{dim}$ = 161 ± 18 Hz, n = 10, p = 0.00054). GPe neuron subtypes also exhibited different responses to hyperpolarizing current injections (Fig. 10*b*). More negative trough potentials were noted in the Npas1$^+$ neurons and Foxp2$^+$ neurons (Npas1$^+$ = −147 ± 17 mV, n = 45; Foxp2$^+$ = −168 ± 8 mV, n = 16) when compared with PV$^+$ neurons (PV$^+$ = −96 ± 7 mV, n = 74, $p < 0.0001$ for both). Within Lhx6$^+$ neurons, Lhx6$^+_{bright}$ neurons and Lhx6$^+_{dim}$ neurons exhibited different trough potentials (Lhx6$^+_{bright}$ = −129 ± 12 mV, n = 24, Lhx6$^+_{dim}$ = −111 ± 13 mV, n = 10, p = 0.010). The trough potential observed in Npas1$^+$-Lhx6$^+$ neurons (Npas1$^+$-Lhx6$^+$ = −119 ± 11 mV, n = 16) was less negative than both Npas1$^+$ neurons (p = 0.0060) and Foxp2$^+$ neurons (p = 0.00091). As seen in previous work from our lab (Hernández et al., 2015), PV$^+$ and PV$^+$-Dbx1$^+$ neurons exhibited the least negative trough potential compared with the other studied GPe neuron types and were not different from one another (PV$^+$ = −96 ± 7 mV, n = 74, PV$^+$-Dbx1$^+$ = −88 ± 16 mV, n = 21, p = 0.24). Dbx1$^+$ neurons had trough potential (Dbx1$^+$ = −104 ± 9 mV, n = 24) more negative than those seen in PV$^+$ neurons (p = 0.0098) and PV$^+$-Dbx1$^+$ neurons (p = 0.0078). Similar to the trough potentials, higher sag ratios were observed for Npas1$^+$ neurons and Foxp2$^+$ neurons (Npas1$^+$ = 1.23 ± 0.13, n = 45; Foxp2$^+$ = 1.33 ± 0.13, n = 16). PV$^+$ neurons had the lowest sag ratio (PV$^+$ = 1.06 ± 0.03, n = 74). Within Lhx6, a difference in the sag ratio was observed between Lhx6$^+_{bright}$ neurons and Lhx6$^+_{dim}$ neurons (Lhx6$^+_{bright}$ = 1.20 ± 0.09, n = 24, Lhx6$^+_{dim}$ = 1.13 ± 0.06, n = 10, p = 0.020). The Npas1$^+$-Lhx6$^+$ neurons exhibited a lower sag ratio than both Npas1$^+$ neurons (Npas1$^+$-Lhx6$^+$ = 1.06 ± 0.04, n = 16, $p < 0.0001$) and Foxp2$^+$ neurons ($p < 0.0001$). As expected, the PV$^+$-Dbx1$^+$ neurons had statistically similar sag ratios to the PV$^+$ neuron population (PV$^+$-Dbx1$^+$ = 1.13 ± 0.08, n = 21, p = 0.19). A full description

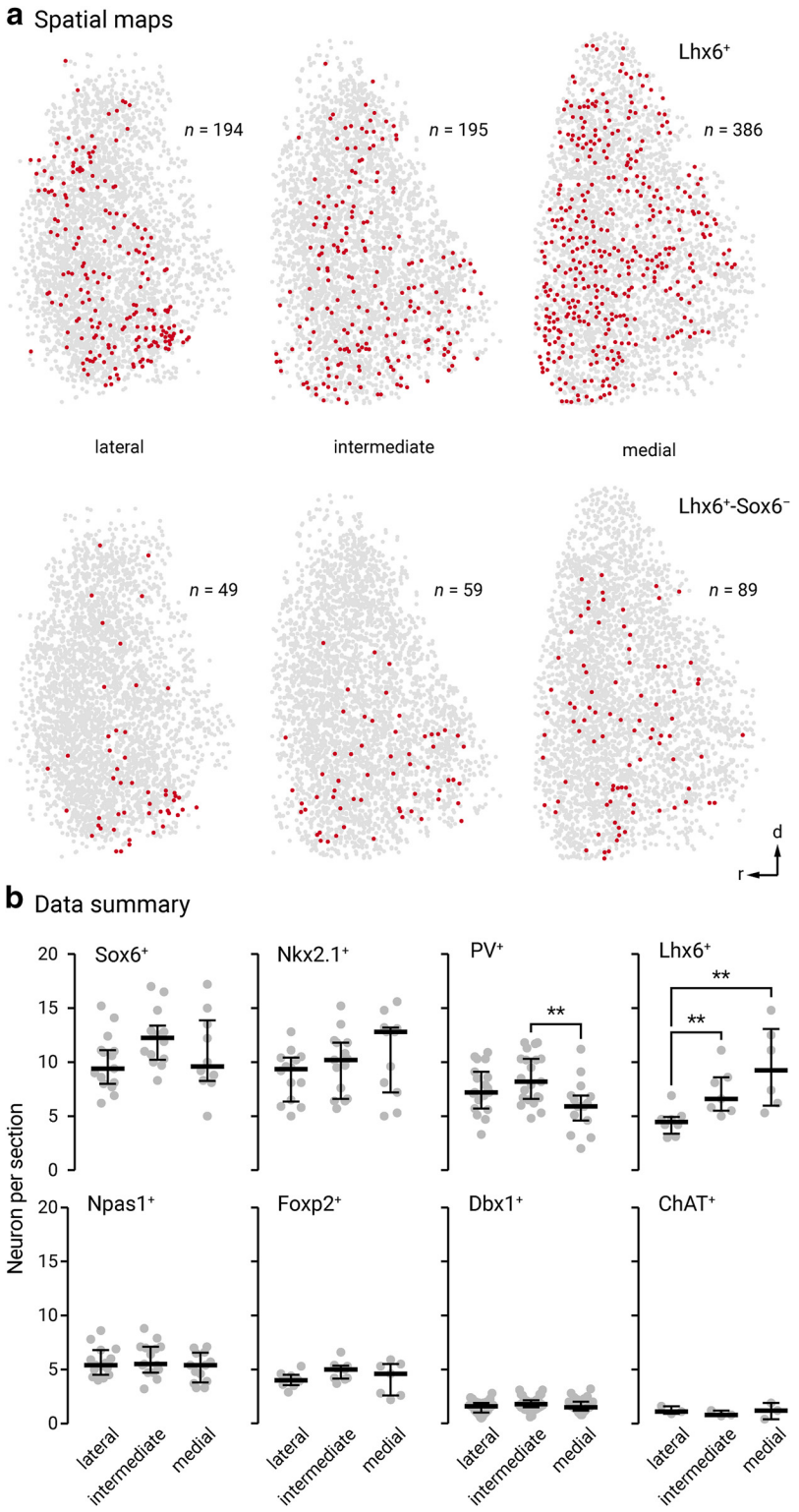

Figure 9. Lateromedial gradients and relative abundance of different GPe neuron classes. ***a***, Spatial maps of the pan-Lhx6$^+$ and unique Lhx6$^+$ Sox6$^-$ GPe neuron populations. Both populations display a lateromedial gradient with more neurons populating the medial GPe. ***b***, Relative abundance of neuron classes in different lateromedial subdivisions of the GPe (Sox6$^+$, lateral: 60 ± 12%, *n*, 4457 neurons, intermediate: 63 ± 11%, *n*, 5112 neurons, medial: 50 ± 11%, *n*, 3286 neurons; Nkx2.1$^+$, lateral: 56 ± 7%, *n*, 3365 neurons, intermediate: 53 ± 9%, *n*, 3878 neurons, medial: 64 ± 14%, *n*, 3265 neurons; PV$^+$, lateral: 46 ± 10%, *n*, 4368 neurons, intermediate: 45 ± 11%, *n*, 5113 neurons, medial: 32 ± 7%, *n*, 2829 neurons; Lhx6$^+$, lateral: 28 ± 6%, *n*, 1422 neurons, intermediate: 42 ± 9%, *n*, 2050 neurons, medial: 45 ± 12%, *n*, 2190 neurons; Npas1$^+$, lateral: 32 ± 6%, *n*, 2635 neurons, intermediate: 31 ± 6%, *n*, 2903 neurons, medial: 27 ± 7%, *n*, 2252 neurons; Foxp2$^+$, lateral: 24 ± 3%, *n*, 939 neurons, intermediate: 26 ± 4%, *n*, 1115 neurons, medial: 25 ± 6%, *n*, 686 neurons; Dbx1$^+$, lateral: 10 ± 2%, *n*, 1219 neurons, intermediate: 9 ± 2%, *n*, 1540 neurons, medial: 8 ± 2%, *n*, 1121 neurons; ChAT$^+$, lateral: 6 ± 1%, *n*, 100 neurons, intermediate: 4 ± 1%, *n*, 76 neurons, medial: 6 ± 3%, *n*, 91 neurons). Percentage total was calculated from HuCD$^+$ cells within each section. Note that PV and Npas1 were expressed in a largely nonoverlapping fashion (2 ± 2%, *n*, 96 neurons, 12 sections). In contrast, considerable overlap between Lhx6 and PV (28 ± 7%, *n*, 654 neurons, 12 sections) or Npas1 (35 ± 5%, *n*, 818 neurons, 12 sections) was observed; the remaining fraction was uniquely labeled with Lhx6. Medians and interquartile ranges are represented in a graphical format. Asterisks denote statistical significance level: $^{**}p < 0.01$, Mann–Whitney *U* test.

of the electrophysiological characteristics of GPe neurons is listed in table form (Table 5).

We wanted to take advantage of the large dataset collected ($n = 556$ neurons) on the spontaneous activity of GPe neurons measured *ex vivo* as it may glean insights into the identification of GPe neurons *in vivo*. In particular, as the spontaneous activity level and regularity (as measured with CV_{ISI}) vary with neuron types, we examined if GPe neurons can be classified into electrophysiological subtypes. *K*-means analysis was implemented as it is one of the simplest and most commonly used strategies (Fig. 10*c*). This analysis returned an optima of $k = 2$ clusters with the centroids at (7.9 Hz, 0.24; $n = 297$ and 18.9 Hz, 0.16; $n = 259$), which approximate to the median values of Npas1$^+$ neurons (8.4 Hz, 0.27) and PV$^+$ neurons (16.7 Hz, 0.14), respectively. The inclusion of additional values for the number of clusters *k* (i.e., 3–6) returned suboptimal clustering as evaluated with silhouette analysis in Figure 10*c*. To evaluate the molecular correspondence of these two mathematically defined clusters, their compositions were visualized. Cluster 1 primarily consisted of PV$^+$ neurons (88.2%) and cluster 2, Npas1$^+$ neurons (63.8%). The mismatch between the molecular identity and the clustering membership assignment was not unexpected based on the population data of spontaneous activity level and regularity (Fig. 10*b*). As Foxp2 neurons are cleanly clustered within cluster 2, this analysis emphasizes the similarity between Npas1$^+$-Nkx2.1$^+$ and PV$^+$ neurons—two primarily MGE-derived populations.

The *k*-means clustering further supports the notion that PV$^+$ neurons and Npas1$^+$ neurons are the two principal neuron classes in the GPe. A logistic regression with PV$^+$ neurons ad Npas1$^+$ neurons as the dependent variable and spontaneous rate and CV_{ISI} as the independent variables showed significant associations for both with neuron type—

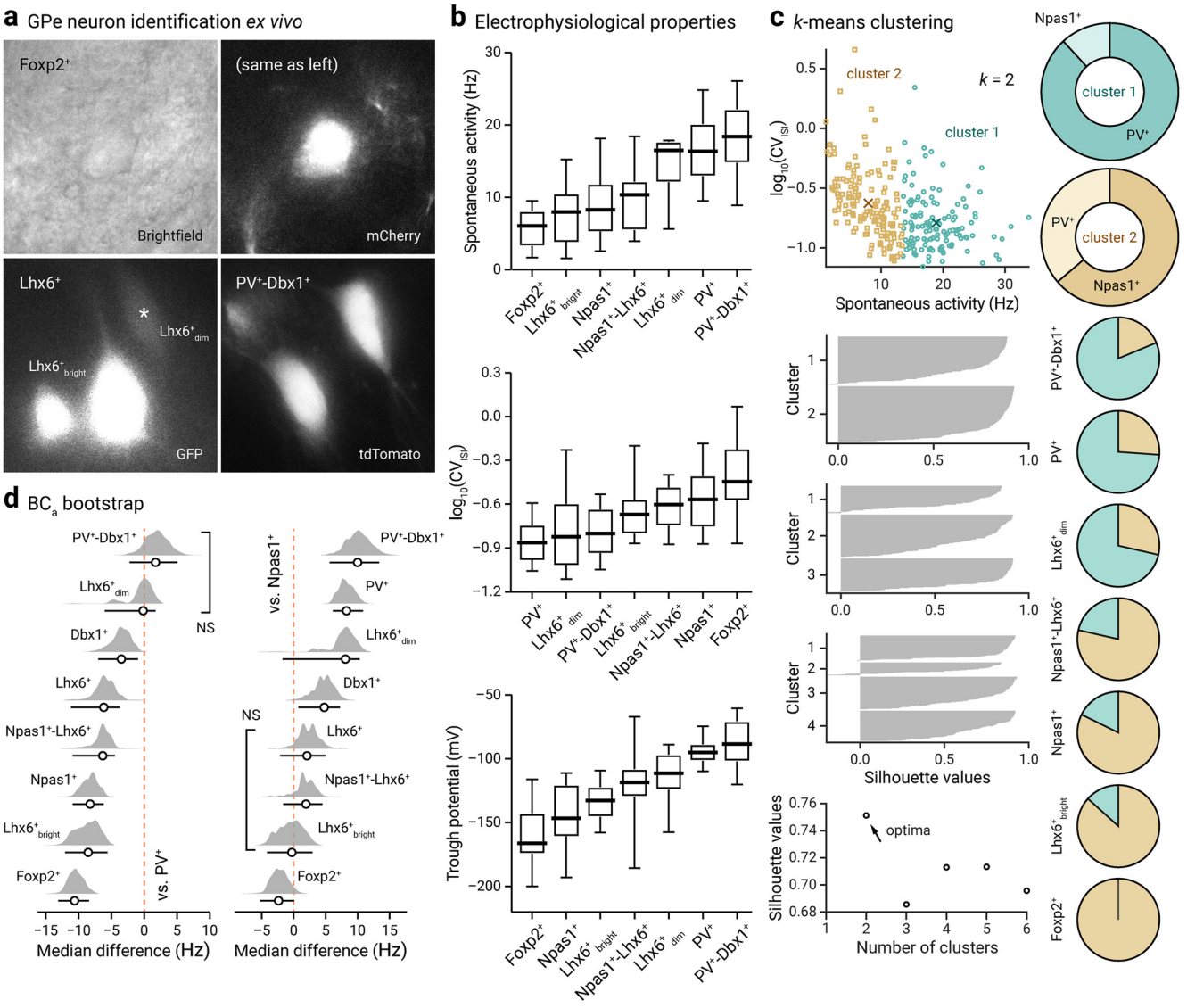

Figure 10. Genetically identified GPe neurons differ in their spontaneous activity. ***a***, Representative bright-field and epifluorescence images of GPe neuron subtypes in *ex vivo* brain slices. Foxp2$^+$ neuron (top, bright-field and mCherry), Lhx6$^+_{bright}$ neurons and Lhx6$^+_{dim}$ (bottom left, GFP), and PV$^+$-Dbx1$^+$ neurons (bottom right, tdTomato) were captured at 60× magnification. Note the difference in the morphology and GFP expression among Lhx6$^+$ neurons. ***b***, Box-plot summary of the electrophysiological properties of identified GPe neuron subtypes. Data are ranked based on the median values. See Tables 5 and 6 for median values, sample sizes, and statistical analysis. Medians, interquartile ranges, and 10th to 90th percentiles are represented in a graphical format. ***c***, Top left, visualization of the clustered data on spontaneous activity (rate and CV_{ISI}) for *k*, 2 clusters. Centroid values for cluster 1 (teal circle) and 2 (tan squares) are as follows: 18.9 Hz, 0.16 and 7.9 Hz, 0.24. Middle left, Silhouette plots for different clusters. Bottom right, Silhouette values are plotted against cluster numbers showing an optima at *k*, 2. Large positive silhouette values indicate that the data point is close to its cluster's centroid, whereas negative silhouette values indicate that the data point is closer to the centroid of the other cluster. Right, a series of pie charts showing the membership assignment of different genetically defined GPe neuron subtypes. The membership assignment in cluster 1 (teal) and 2 (tan) for each neuron subtypes are as follows: PV$^+$-Dbx1$^+$ (81.3%, 18.8%, *n*, 16), PV$^+$ (73.9%, 26.1%, *n*, 111), Lhx6$^+_{dim}$ (71.4%, 28.6%, *n*, 7), Npas1$^+$-Lhx6$^+$ (21.4%, 78.6%, *n*, 14), Npas1$^+$ (17.7%, 82.3%, *n*, 62), Lhx6$^+_{bright}$ (13.3%, 86.7%, *n*, 15), Foxp2$^+$ (0.0%, 100.0%, *n*, 20). Data are not shown for Dbx1$^+$ (50.0%, 50.0%, *n*, 20) and Lhx6$^+$ (61.1%, 38.9%, *n*, 18), which both contain a mixture of PV$^+$ neurons and Npas1$^+$ neurons. ***d***, Bias-corrected and accelerated (BC_a) bootstrap estimation of effect sizes (median differences) and 95% confidence intervals. The median difference in spontaneous rate for seven comparisons against the PV$^+$ neurons (left) and Npas1$^+$ neurons (right) are shown. Median differences are plotted as bootstrap sampling distributions. Each median difference is depicted as a circle. Median differences are also encoded by color saturation. Lower and upper confidence interval bounds are indicated by the horizontal bars. Lhx6$^+_{dim}$ neurons and PV$^+$-Dbx1$^+$ neurons are statistically nonsignificant from PV$^+$ neurons (*p*, 0.45 and 0.24). Lhx6$^+_{bright}$ neurons, Npas1$^+$-Lhx6$^+$ neurons, and Lhx6$^+$ neurons are statistically nonsignificant from Npas1$^+$ neurons (p = 0.44, 0.29, and 0.066).

estimated odds ratio of 1.26 for spontaneous rate, $p < 0.0001$, indicating a higher value in PV$^+$ neurons; estimated odds ratio of 0.08 for CV_{ISI}, $p = 0.0020$, indicating a higher value in Npas1$^+$ neurons. As logistic regression indicates a strong association between spontaneous activity level and neuron type, bootstrap analysis was applied to estimate the differences between genetically-defined neuron subtypes and these two principal neuron classes (Fig. 10*d*). In general, 9 of the 10 characteristics considered—all except for AP height—showed differences among cell types based on the Kruskal–Wallis test, even after the Bonferroni multiple testing correction. It is notable that Npas1$^+$-Lhx6$^+$ neurons and Lhx6$^+_{bright}$ neurons have spontaneous activity that is statistically nonsignificant from Npas1$^+$ neurons (p = 0.29 and 0.44, respectively). Furthermore, Dbx1$^+$-PV$^+$ neurons and Lhx6$^+_{dim}$ neurons exhibited spontaneous activity consistent with canonical PV$^+$ neuron (p = 0.24 and 0.45, respectively). Pair-

Table 5. Electrophysiological characteristics of GPe neurons

	Molecularly defined neuron types																			
	PV$^+$		Npas1$^+$		Foxp2$^+$		Lhx6$^+$		Lhx6$^+_{dim}$		Lhx6$^+_{bright}$		Dbx1$^+$		PV$^+$-Dbx1$^+$		Npas1$^+$-Lhx6$^+$	
	Median ± MAD	n^a	Median ± MAD	n	Median ± MAD	n	Median ± MAD	n	Median ± MAD	n	Median ± MAD	n	Median ± MAD	n	Median ± MAD	n	Median ± MAD	n
Spontaneous activity (Hz)	16.7 ± 3.4	111	8.4 ± 3.1	63	6.1 ± 1.9	20	10.5 ± 5.1	43	16.5 ± 1.2	7	8.1 ± 2.7	18	13.2 ± 2.7	21	18.4 ± 3.6	16	10.4 ± 2.8	14
CV_{ISI}	0.14 ± 0.03	111	0.27 ± 0.10	63	0.36 ± 0.09	20	0.21 ± 0.07	43	0.15 ± 0.07	7	0.21 ± 0.04	18	0.14 ± 0.03	21	0.16 ± 0.05	16	0.25 ± 0.07	14
Max rate (Hz)	198 ± 24	49	96 ± 34	33	55 ± 23	16	106 ± 36	49	161 ± 18	10	93 ± 31	24	180 ± 27	24	164 ± 30	21	–	–
Max current (pA)	1140 ± 260	49	240 ± 160	33	160 ± 90	16	340 ± 200	49	840 ± 370	10	310 ± 170	24	880 ± 250	24	700 ± 300	21	–	–
Membrane potential (mV)	−56 ± 3	41	−51 ± 3	24	−48 ± 7	16	−50 ± 4	34	−43 ± 1	10	−52 ± 3	24	−54 ± 3	24	−51 ± 3	21		
Trough potential (mV)	−96 ± 7	74	−147 ± 17	45	−168 ± 8	16	−122 ± 17	63	−111 ± 13	10	−129 ± 12	24	−104 ± 9	24	−88 ± 16	21	−119 ± 11	16
Sag ratio	1.06 ± 0.03	74	1.23 ± 0.13	45	1.33 ± 0.13	16	1.13 ± 0.06	63	1.13 ± 0.06	10	1.20 ± 0.09	24	1.14 ± 0.07	24	1.13 ± 0.08	21	1.06 ± 0.04	16
First/last ISI ratio	0.79 ± 0.05	49	0.61 ± 0.05	33	0.63 ± 0.06	16	0.67 ± 0.06	49	0.68 ± 0.04	10	0.66 ± 0.07	24	0.71 ± 0.07	24	0.69 ± 0.03	21	–	–
AP height (mV)	67 ± 7	41	63 ± 9	24	67 ± 8	16	63 ± 8	34	62 ± 5	10	64 ± 9	24	64 ± 4	24	60 ± 3	21	–	–
AP width (ms)	0.67 ± 0.06	41	1.11 ± 0.23	24	1.24 ± 0.33	16	0.95 ± 0.16	34	0.74 ± 0.08	10	0.99 ± 0.17	24	0.70 ± 0.06	24	0.77 ± 0.12	21	–	–

[a]*n* value equals number of neurons.

AP, Action potential; CV, coefficient of variation; ISI, interspike interval; MAD, median absolute deviation.

Table 6. Statistical analysis for electrophysiological characteristics

		Pairwise comparisons[a]																
	Kruskal–Wallis	PV$^+$ vs PV$^+$-Dbx1$^+$	PV$^+$ vs Npas1$^+$	PV$^+$ vs Lhx6$^+$	PV$^+$ vs Foxp2$^+$	PV$^+$ vs Dbx1$^+$	Npas1$^+$ vs Lhx6$^+$	Npas1$^+$ vs Foxp2$^+$	Npas1$^+$ vs Dbx1$^+$	Npas1$^+$ vs PV$^+$-Dbx1$^+$	Foxp2$^+$ vs Lhx6$^+$	Lhx6$^+$ vs Dbx1$^+$	Lhx6$^+$ vs PV$^+$-Dbx1$^+$	Foxp2$^+$ vs Dbx1$^+$	Foxp2$^+$ vs PV$^+$-Dbx1$^+$	Dbx1$^+$ vs PV$^+$-Dbx1$^+$	Npas1$^+$-Lhx6$^+$ vs PV$^+$	Npas1$^+$-Lhx6$^+$ vs Npas1$^+$
Spontaneous activity (Hz)	**<0.0001**	0.24	**<0.0001**	**<0.0001**	**<0.0001**	0.0080	0.066	0.016	0.0070	**<0.0001**	0.00090	0.11	**0.00011**	**<0.0001**	**<0.0001**	0.011	**0.00014**	0.29
CV_{ISI}	**<0.0001**	0.21	**<0.0001**	**<0.0001**	**<0.0001**	0.24	0.073	0.067	**<0.0001**	0.00072	0.0065	0.0070	0.019	**<0.0001**	**<0.0001**	0.44	**<0.0001**	0.43
Max rate (Hz)	**<0.0001**	0.014	**<0.0001**	**<0.0001**	**<0.0001**	0.074	0.12	0.094	**<0.0001**	**<0.0001**	0.010	**<0.0001**	0.0010	**<0.0001**	**<0.0001**	0.24	NA	NA
Max current (pA)	**<0.0001**	0.0035	**<0.0001**	**<0.0001**	**<0.0001**	0.013	0.054	0.091	**<0.0001**	**0.00011**	0.0038	**0.00049**	0.0050	**<0.0001**	**<0.0001**	0.31	NA	NA
Membrane potential (mV)	**0.0011**	0.012	0.032	**<0.0001**	0.0021	0.29	0.060	0.13	0.12	0.34	0.43	0.0025	0.15	0.015	0.23	0.062	NA	NA
Trough potential (mV)	**<0.0001**	0.24	**<0.0001**	**<0.0001**	**<0.0001**	0.0098	0.00086	0.10	**<0.0001**	**<0.0001**	**0.00024**	0.014	**<0.0001**	**<0.0001**	**<0.0001**	0.0078	**0.00027**	0.0060
Sag ratio	**<0.0001**	0.19	**<0.0001**	0.00019	**<0.0001**	**0.00011**	0.0034	0.055	0.14	**0.00026**	**0.00019**	0.14	0.062	0.011	**<0.0001**	0.015	0.49	**<0.0001**
First/last IS ratio	**<0.0001**	0.0010	**<0.0001**	**<0.0001**	**<0.0001**	0.0087	0.0023	0.22	**0.00015**	0.0033	0.080	0.092	0.32	0.011	0.056	0.24	NA	NA
AP height (mV)	0.093	0.0046	0.27	0.18	0.33	0.070	0.41	0.19	0.22	0.035	0.13	0.27	0.041	0.058	0.0063	0.14	NA	NA
AP width (ms)	**<0.0001**	0.025	**<0.0001**	**<0.0001**	**<0.0001**	0.074	0.10	0.24	**<0.0001**	**<0.0001**	0.032	**0.00021**	0.0020	**<0.0001**	**<0.0001**	0.30	NA	NA

	Kruskal-Wallis	Npas1$^+$-Lhx6$^+$ vs Foxp2$^+$	Npas1$^+$-Lhx6$^+$ vs Dbx1$^+$	Npas1$^+$-Lhx6$^+$ vs PV$^+$-Dbx1$^+$	Lhx6$^+_{bright}$ vs Npas1$^+$	Lhx6$^+_{dim}$ vs Npas1$^+$	Lhx6$^+_{bright}$ vs PV$^+$	Lhx6$^+_{dim}$ vs PV$^+$	Lhx6$^+_{bright}$ vs Foxp2$^+$	Lhx6$^+_{dim}$ vs Foxp2$^+$	Lhx6$^+_{bright}$ vs Dbx1$^+$	Lhx6$^+_{dim}$ vs Dbx1$^+$	Lhx6$^+_{bright}$ vs PV$^+$-Dbx1$^+$	Lhx6$^+_{dim}$ vs PV$^+$-Dbx1$^+$	Lhx6$^+_{bright}$ vs Npas1$^+$-Lhx6$^+$	Lhx6$^+_{dim}$ vs Npas1$^+$-Lhx6$^+$	Lhx6$^+_{bright}$ vs Lhx6$^+_{dim}$
Spontaneous activity (Hz)	**<0.0001**	0.021	0.092	0.00044	0.44	0.014	**<0.0001**	0.45	0.14	**0.00041**	0.0013	0.19	**<0.0001**	0.17	0.17	0.020	0.0039
CV_{ISI}	**<0.0001**	0.11	0.0049	0.011	0.22	0.060	**0.00015**	0.54	0.0070	0.011	0.0063	0.79	0.050	1.0	0.51	0.15	0.33
Max rate (Hz)	**<0.0001**	NA	NA	NA	0.95	0.00048	**<0.0001**	0.0051	0.040	**<0.0001**	**<0.0001**	0.24	**<0.0001**	0.78	NA	NA	0.00054
Max current (pA)	**<0.0001**	NA	NA	NA	0.44	**0.00034**	**<0.0001**	0.028	0.011	**0.00016**	**<0.0001**	0.98	**0.00038**	0.50	NA	NA	0.0016
Membrane potential (mV)	**0.001**	NA	NA	NA	0.99	**<0.0001**	0.072	**<0.0001**	0.28	0.087	0.18	**<0.0001**	0.85	**<0.0001**	NA	NA	**<0.0001**
Trough potential (mV)	**<0.0001**	0.00091	0.11	0.00034	0.039	0.00088	**<0.0001**	0.013	0.00048	**0.00082**	**<0.0001**	0.64	**<0.0001**	0.0088	0.058	0.34	0.010
Sag ratio	**<0.0001**	**<0.0001**	0.0033	0.25	0.58	0.025	**<0.0001**	0.14	0.026	0.0010	0.21	0.17	0.0019	0.69	**<0.0001**	0.27	0.020
First/last ISI ratio	**<0.0001**	NA	NA	NA	0.020	0.0058	**<0.0001**	**0.00039**	0.27	0.097	0.16	0.31	0.36	0.70	NA	NA	0.62
AP height (mV)	0.093	NA	NA	NA	0.94	0.72	0.76	0.21	0.44	0.26	0.43	0.75	0.13	0.44	NA	NA	0.70
AP width (ms)	**<0.0001**	NA	NA	NA	0.41	0.0047	**<0.0001**	0.010	0.044	0.0030	**<0.0001**	0.16	**<0.0001**	0.49	NA	NA	0.012

[a]Two-tailed *p* values are listed. The first column represents *p*-values from Kruskal–Wallis tests comparing each characteristic across all groups, with the Lhx6 neurons all grouped together; the second set of columns give *p*-values from Dunn tests comparing each pair of neuron types, with the Lhx6 neurons all grouped together; the third set of columns give *p*-values from Mann–Whitney tests comparing the Lhx6$^+_{bright}$ and Lhx6$^+_{dim}$ neuron subtypes with all other neuron types. The bolded *p*-values are significant when considering the Bonferroni-corrected thresholds, which are equivalent to 0.05/10, 0.05/170, and 0.05/118, respectively.

AP, Action potential; CV, coefficient of variation; ISI, interspike interval; MAD, median absolute deviation.

wise comparisons of the electrophysiological characteristics across molecularly defined GPe neuron subtypes are tabulated in Table 6.

As multiple electrophysiological characteristics were obtained, we asked whether a combination of these quantitative features can statistically define GPe neurons. To determine at the single-cell level whether genetically-defined GPe neuron subtypes form separate or overlapping clusters, we applied a principal component analysis to the electrophysiological dataset (Fig. 11). Neurons with incomplete data were excluded from the analysis. As expected, and as illustrated by the dendrogram, neurons defined by PV and Npas1 transgenic lines were completely separated. Accordingly, they exhibited unique electrophysiological signatures as illustrated by the heatmap (Fig. 11*a*). This analysis established the correspondence of electrophysiological classes with predefined markers, i.e., PV and Npas1. Moreover, different genetically-defined GPe neurons that were targeted in this study have electrophysiological properties that can be broadly categorized into either PV$^+$ neuron or Npas1$^+$ neuron classes. This analysis reaffirmed our previous assertion regarding the utility of these transgenic lines and markers (Hernández et al., 2015). Though electrophysiological differences exist between Npas1$^+$ neuron subclasses, hierarchical clustering of electrophysiological properties was insufficient to define GPe neuron subclasses.

The *k*-means and hierarchical clustering analyses provide complementary points of view for exploring our rich dataset. We used *k*-means with only spontaneous activity level and variability as the clustering variables, as they have the least amount of missing data, leading to a large dataset ($n = 556$ neurons). In addition, activity level and patterns have obvious appeal as they may glean new insights into the classification of GPe neurons *in vivo*. *k*-means clustering with these two variables thus provides a powerful and convenient visualization of the data. Although hierarchical clustering provides clusters by using more variables, it is not immediately apparent how each electrophysiological characteristic relates to the clusters.

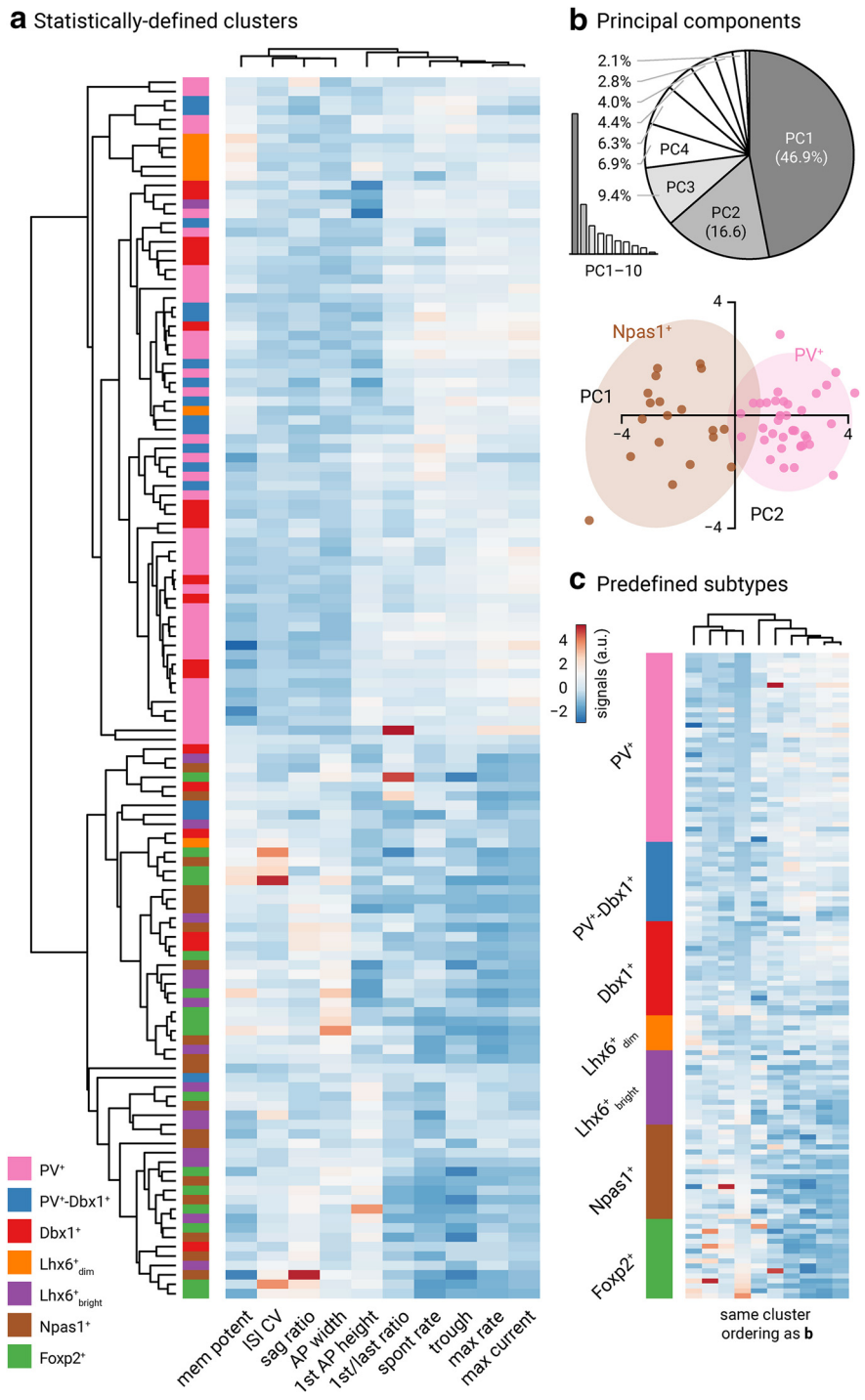

Figure 11. Electrophysiological multivariate analysis of GPe neurons. ***a***, Heatmap representation of electrical signatures of genetically identified GPe neuron subtypes. Dendrograms show the order and distances of neuron clusters and their electrical characteristics. A total of 130 neurons (*n*, PV$^+$: 38, Npas1$^+$: 19, Dbx1$^+$: 19, Foxp2$^+$: 16, PV$^+$-Dbx1$^+$: 16, Lhx6$^+_{bright}$: 16, Lhx6$^+_{dim}$: 7) were included in this analysis. Neurons with incomplete data were excluded from the analysis. ***b***, Top, Scree plot (left) and pie chart (right) showing that the first three principal components (gray) capture 72.9% of the total variability in the data. Bottom, Principal component 1 and 2 account for 46.9% and 16.6% of the total variance, respectively. Prediction ellipses for PV$^+$ neurons (pink) and Npas1$^+$ neurons (brown) are shown. With probability 0.95, a new observation from the same group will fall inside the ellipse. ***c***, Same dataset as ***a***. Data are sorted by genetically identified neuron subtypes. Ordering of the clustering is the same as ***a***.

Discussion

In this study, we generated a more comprehensive landscape of GPe neuron composition. Specifically, we provided a more complete investigation of the Lhx6$^+$ and Dbx1$^+$ populations, along with novel insight into the properties of neurons arising from the Sox6 lineage. We were able to molecularly define the entirety of Lhx6$^+$ neurons (Table 3), thus resolving one of the debates in the field. Overall, our data further support the idea that PV$^+$ neurons and Npas1$^+$ neurons are two principal neuron classes. Our current study further illustrates the complexity of GPe neurons in adult mice and infers the existence of new neuron subclasses within Npas1$^+$ neuron classes. Based on the molecular, anatomical, and intrinsic properties, our results support the idea that Npas1$^+$-Nkx2.1$^+$ neurons are a distinct GPe neuron subclass (Fig. 12).

Classification of GPe neurons

Heterogeneity in the phenotype of GPe neurons was noted in the early 70's (DeLong, 1971; Fox et al., 1974). The descriptions of molecularly defined GPe neuron subtypes were not established until less than a decade ago (Flandin et al., 2010; Nóbrega-Pereira et al., 2010). Our group has extended previous findings that PV$^+$ neurons and Npas1$^+$ neurons represent the two principal neuron classes in the adult GPe. Specifically, these two neuron classes are distinct across multiple modalities, including axonal patterns, electrophysiological properties, and alterations in disease states (Hernández et al., 2015; Glajch et al., 2016; Hegeman et al., 2016). Our unpublished observations continue to support this notion. On the other hand, other groups have adopted different, though not mutually exclusive, classification schemes.

Within the Npas1$^+$ class, Foxp2$^+$ neurons (Npas1$^+$-Foxp2$^+$, aka arkypallidal neurons) represent the first unique GPe neuron subclass to be described. This idea is supported by compelling data showing their distinct features, such as developmental origin, electrophysiological, anatomical, and molecular profiles (Dodson et al., 2015). Based on relative spike timing across basal ganglia nuclei in an operant behavioral task, it has been proposed that Npas1$^+$-Foxp2$^+$ neurons are important for motor suppression (Mallet et al., 2016). Meanwhile, the makeup of the remaining neurons in the GPe has been elusive. They are commonly referred to as prototypic neurons. We, and others, noted that prototypic neurons are not simply a single class of neurons (Flandin et al., 2010; Nóbrega-Pereira et al., 2010; Mastro et al., 2014; Abdi et al., 2015; Dodson et al., 2015; Hernández et al., 2015; Saunders et al., 2015; Oh et al., 2017; Abrahao and Lovinger, 2018; Hunt et al., 2018; Saunders et al., 2018). Instead, this group encompasses a heterogeneous population of neurons, and their properties have not been

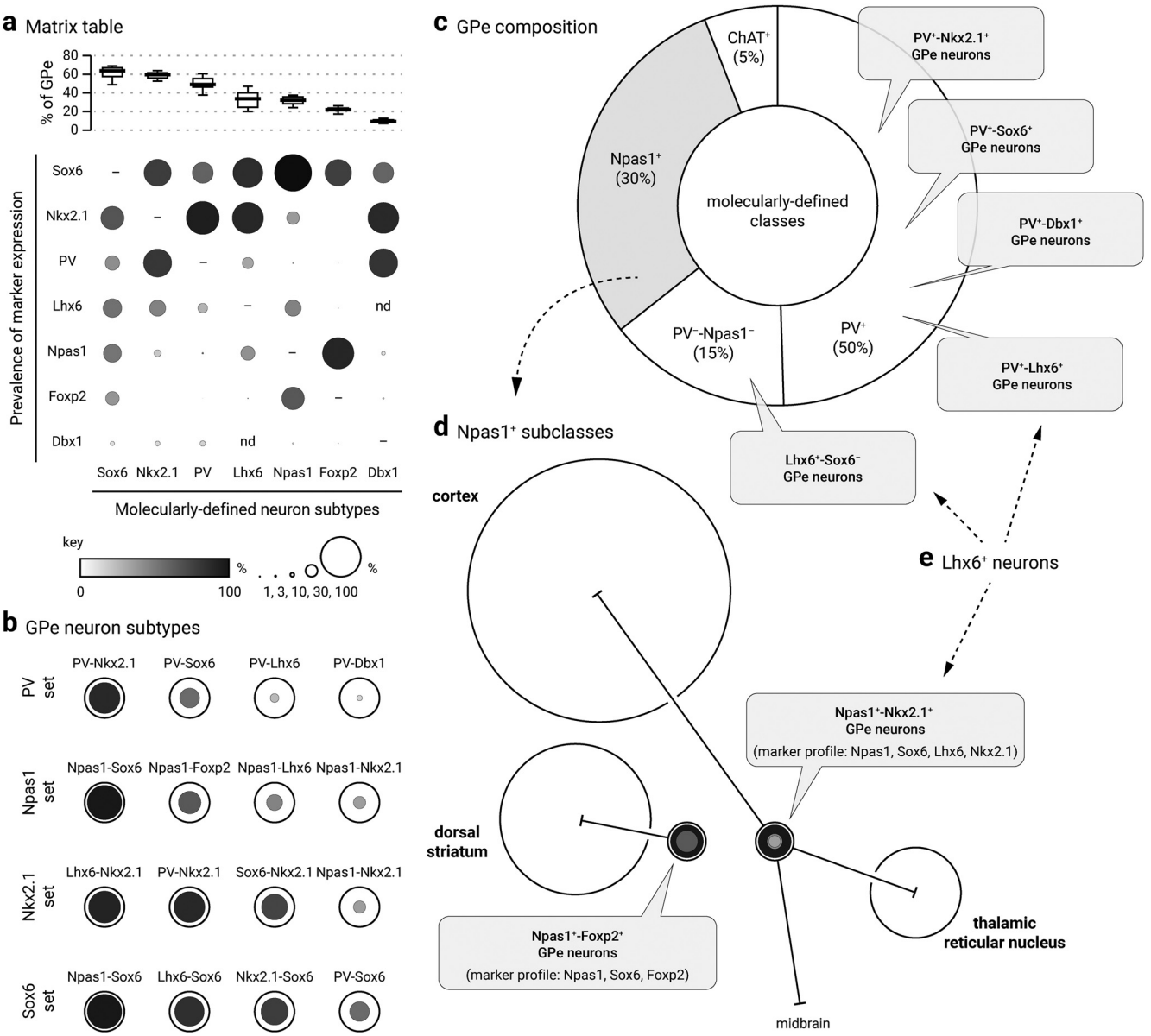

Figure 12. Diagrams summarizing the marker expression profile and classification scheme derived from the current study. ***a***, Data from Table 3 are graphically represented to convey the coexpression of markers (vertical axis) within each molecularly defined neuron subtype (horizontal axis). As visualized at the top of the matrix table, medians are presented as thick horizontal lines (Fig. 1) and data are sorted according to the abundance of neuron subtypes within the GPe. Both the size and grayscale intensity of each circle represents the prevalence of expression within specific GPe neuron subtypes. Circles along each column do not add up to 100% as there is overlapping marker expression with each neuron subtype. —, Not shown; nd, not determined. For example, Foxp2 (sixth row) is selectively expressed in Npas1 neurons and a subset of Sox6 neurons; it is absent in Nkx2.1$^+$ and PV$^+$ neurons. Within the Foxp2$^+$ population (sixth column), Sox6 and Npas1 are the only markers expressed. The high prevalence of Npas1 and Sox6 within the Foxp2$^+$ neuron subtype (sixth column) is demonstrated by larger and darker circles. Note that because Foxp2 and Nkx2.1 are nonoverlapping, there is no circle for Nkx2.1. Accordingly, Npas1$^+$-Foxp2$^+$ subclass and Npas1$^+$-Nkx2.1$^+$ subclass represent 57% and 32% of the Npas1$^+$ population, respectively. As a comparison, Sox6 (first row) is expressed across all identified neuron types. Sox6 expression (first row) was observed in a major fraction of each population, especially Npas1$^+$ neurons. The Sox6 neuron subtype (first column) expresses a broader range of markers. Last, neurons from the Dbx1 lineage (seventh row) are heterogeneous and overall contribute to only a small fraction of each molecularly defined neuron subtype. ***b***, Summary of the GPe neuron classification based on the expression profile of different molecular markers, i.e., data from ***a***. ***c***, Pie chart summarizing the neuronal composition of the mouse GPe. The area of the sectors represents the approximate size of each neuron class. PV$^+$ neurons (which constitute 50% of the GPe) are heterogeneous. Nkx2.1, Sox6, Lhx6, and Dbx1 are coexpressed in PV$^+$ neurons to a varying extent. How they intersect with each other remains to be determined. Npas1$^+$ neurons (gray) are 30% of the GPe; they can be subdivided into two subclasses (see ***d***). ChAT$^+$ neurons are ~5% of the total GPe neuron population and show no overlap with other known classes of GPe neurons. ***d***, Two *bona fide* subclasses of Npas1$^+$ neurons (Npas1$^+$-Foxp2$^+$ and Npas1$^+$-Nkx2.1$^+$) are identified in the mouse GPe. They differ in their molecular marker expression, axonal projections, and electrophysiological properties. Although Npas1$^+$-Foxp2$^+$ neurons project to the dorsal striatum, Npas1$^+$-Nkx2.1$^+$ neurons project to the cortex, thalamus, and mid/hindbrain areas. Size of the target areas (circles) is an artistic rendering based on the volume of those areas, but not the axonal density, synaptic strength, or contacts formed by Npas1$^+$ neuron subclasses. ***e***, Lhx6$^+$ neurons are highlighted. Both PV$^+$-Lhx6$^+$ neurons and Npas1$^+$-Lhx6$^+$ neurons coexpress Sox6. Lhx6$^+$-Sox6$^-$ neurons are a subset of PV$^-$-Npas1$^-$ neurons.

fully described. Our incomplete understanding of these neurons has prevented us from appreciating how individual neuron subclasses are precisely involved in motor function and dysfunction. Here, we found that Npas1$^+$-Foxp2$^+$ neurons are distinct from Npas1$^+$-Nkx2.1$^+$ neurons. Accordingly, both of them should be regarded as *bona fide* subclasses.

The examination of the molecular profiles of GPe neurons hinted at the diversity of PV$^+$ neurons. Yet, we do not have

sufficient data to argue if they fall into different neuron subclasses. Based on enhancer/transgenic mice, Silberberg and colleagues (Silberberg et al., 2016) suggest the existence of two pools of PV$^+$ neurons that are produced with different temporal patterns and occupy slightly different, but otherwise largely overlapping spatial domains within the GPe. Consistent with this observation, more recent single-cell transcriptomic analysis confirms the existence of four major neuron types in the GPe, including two PV$^+$ neuron clusters, in addition to two distinct Npas1$^+$ neuron clusters (Saunders et al., 2018). It is paramount to determine whether they constitute distinct functional subclasses. These efforts will, in turn, give meaning to otherwise arbitrary classifications.

Toward a more complete description of the GPe

We hypothesized the existence of a unique population of Lhx6$^+$ neurons (i.e., Lhx6$^+$-PV$^-$-Npas1$^-$) that accounts for at least 15% of GPe neurons. This idea is supported by our data along with data from others (Mastro et al., 2014; Dodson et al., 2015; Hernández et al., 2015; Hegeman et al., 2016). In this study, we first examined the expression of Nkx2.1, Lhx6, and Sox6 among GPe neurons, as these transcription factors work in concert to dictate cell fate during development. As Sox6 is described as MGE-enriched, one would expect its expression in all Lhx6$^+$ neurons. The examination of Sox6 expression unequivocally confirmed the existence of this unique Lhx6$^+$ population—however, to our surprise, this unique Lhx6$^+$ population is Sox6$^-$. Importantly, our results resolve some of the discrepancies related to Lhx6$^+$ neurons and identify the PV$^-$ and Npas1$^-$ neurons described in our previous study (Mastro et al., 2014; Dodson et al., 2015; Hernández et al., 2015; Hegeman et al., 2016).

Although Dbx1$^+$ neurons that originate from the PoA are known to populate the GPe (Gelman et al., 2009; Nóbrega-Pereira et al., 2010), their properties were not fully determined. We examined whether Dbx1$^+$ neurons correspond to the Lhx6$^+$-Sox6$^-$ population. Contrary to our hypothesis, our data argue that Dbx1$^+$ neurons do not correspond to this population of neurons. Instead, we found the Dbx1$^+$ population contains neurons that express, to varying degrees, all established GPe neuron markers (Fig. 2, Table 3). This is consistent with the literature that PoA progenitors give rise to a small, but diverse, contingent set of neurons (Gelman et al., 2009, 2011). In particular, most Dbx1$^+$ neurons are Sox6$^+$, and they primarily express PV$^+$ or Npas1$^+$. In hindsight, these results were not completely unexpected. Although the embryonic PoA is similar to the MGE in that it expresses the transcription factor Nkx2.1, many PoA cells do not express Lhx6 (Flames et al., 2007). It has been shown that a subset of LGE (lateral ganglionic eminence) progenitors express Lhx6 (Liodis et al., 2007). Importantly, the LGE is known to generate GABAergic neurons that populate the cortex (de Carlos et al., 1996; Tamamaki et al., 1997; Anderson et al., 2001; Jiménez et al., 2002). Therefore, it is possible that the Lhx6$^+$-Sox6$^-$ GPe population arises from the LGE. One limitation with using the Lhx6-GFP mouse, which is a BAC transgenic line, is the concern that GFP is expressed in ectopic neurons. However, given the near complete overlap with Nkx2.1, we are confident that its expression is accurate within the GPe. We await new tools that give us unique access to the Lhx6$^+$-Sox6$^-$ population. It is interesting to see that PV$^+$-Dbx1$^+$ neurons display a phenotype that is shared with the general PV$^+$ population, which originate primarily from the MGE (Flandin et al., 2010; Nóbrega-Pereira et al., 2010). Although the extent of the overlap remains to be fully established, our findings are in line with what was shown previously that neurons that arise from spatially distinct ontogenic domains can converge onto a single neuron class (Chittajallu et al., 2013). However, cellular phenotypes, such as transcriptomic program and electrophysiological profiles, can be shaped by neuromodulatory signals. It is intriguing to hypothesize that brain states, imposed by various neuromodulatory signals, may have differential impacts on these neuron subtypes as a result of distinct receptor profiles. High-throughput single-cell transcriptomic analysis has become an extremely powerful tool for cell classification. However, as both Lhx6$^+$-Sox6$^-$ and Dbx1$^+$ neurons are sparse in the GPe, they are likely underrepresented in previous single-cell transcriptomic studies (Saunders et al., 2018; Zeisel et al., 2018). Our current study has thus provided important insight into these low abundance neurons.

Significance of the cortico-pallido-cortical loop

Though our connectome survey did not reveal either Lhx6$^+$-Sox6$^-$ neurons or Dbx1$^+$ neurons to be cortically projecting, it pinpointed Npas1$^+$-Nkx2.1$^+$ neurons as key constituents of the cortico-pallido-cortical loop. This finding can have far-reaching implications in motor planning, motor learning, and decision making (Ito and Doya, 2011; Barthas and Kwan, 2017; Hanks and Summerfield, 2017; Abs et al., 2018; Papale and Hooks, 2018; Svoboda and Li, 2018). We noted that the GPe innervation is not a consistent feature of all PT neurons (Cowan and Wilson, 1994; Kita and Kita, 2012; Shepherd, 2014; Shibata et al., 2018), this is likely related to the rich diversity of cortical neuron subtypes (Gouwens et al., 2019).

Importantly, recent data have shown that the electrophysiological activity of primate PT neurons is altered in the parkinsonian state (Pasquereau and Turner, 2011). Our results provide insight into a potential cellular mechanism that underlies the effectiveness of deep brain stimulation (DBS), which involves the implantation of a frequency stimulation electrode in the STN. DBS has emerged as a crucial adjunct to manage the motor symptoms of PD (Wichmann and Delong, 2006; Wichmann et al., 2018). The present results suggest that activation of cortical axons during DBS may activate brain sites innervated by the multiprojectional PT-type cortical neurons. Activation of these brain regions, including the GPe, may contribute to the alleviation of motor symptoms with DBS.

Concluding remarks

In this study, we have performed a thorough characterization of GPe neuron populations according to their expression of genetic markers, electrophysiological properties, and anatomical projections. In addition, we have attempted to characterize and employ various novel driver and reporter lines. We hope that our findings will facilitate cross-laboratory utilization of standard tools to study GPe neuron types. The identification of GPe neuron populations should allow experiments to be conducted on the same neuron type across subjects and laboratories. Examining the same (i.e., homologous) neuron population across species facilitates comparative studies; commonalities and differences in phenotype could then be linked to behavior. As we have completed cataloging major neuron types within the GPe, our next goal is to use intersectional tools to define constituent neuron subclasses and their functions. We have used similar strategies in this study and also recently in Poulin et al. (Poulin et al., 2018). The generation and identification of additional Flp driver lines will likely be helpful for the interrogation of GPe neuron diversity and func-

tion. Ultimately, our goal is to identify single recombinase driver lines that efficiently capture functional neuron subclasses.

References

Abdi A, Mallet N, Mohamed FY, Sharott A, Dodson PD, Nakamura KC, Suri S, Avery SV, Larvin JT, Garas FN, Garas SN, Vinciati F, Morin S, Bezard E, Baufreton J, Magill PJ (2015) Prototypic and arkypallidal neurons in the dopamine-intact external globus pallidus. J Neurosci 35:6667–6688.

Abrahao KP, Lovinger DM (2018) Classification of GABAergic neuron subtypes from the globus pallidus using wild-type and transgenic mice. J Physiol 596:4219–4235.

Abs E, Poorthuis RB, Apelblat D, Muhammad K, Pardi MB, Enke L, Kushinsky D, Pu DL, Eizinger MF, Conzelmann KK, Spiegel I, Letzkus JJ (2018) Learning-related plasticity in dendrite-targeting layer 1 interneurons. Neuron 100:684–699.e6.

Ährlund-Richter S, Xuan Y, van Lunteren JA, Kim H, Ortiz C, Pollak Dorocic I, Meletis K, Carlén M (2019) A whole-brain atlas of monosynaptic input targeting four different cell types in the medial prefrontal cortex of the mouse. Nat Neurosci 22:657–668.

Anderson ME, Horak FB (1985) Influence of the globus pallidus on arm movements in monkeys. III. Timing of movement-related information. J Neurophysiol 54:433–448.

Anderson SA, Marín O, Horn C, Jennings K, Rubenstein JL (2001) Distinct cortical migrations from the medial and lateral ganglionic eminences. Development 128:353–363.

Asanuma C (1989) Axonal arborizations of a magnocellular basal nucleus input and their relation to the neurons in the thalamic reticular nucleus of rats. Proc Natl Acad Sci U S A 86:4746–4750.

Asanuma C (1994) GABAergic and pallidal terminals in the thalamic reticular nucleus of squirrel monkeys. Exp Brain Res 101:439–451.

Azim E, Jabaudon D, Fame RM, Macklis JD (2009) SOX6 controls dorsal progenitor identity and interneuron diversity during neocortical development. Nat Neurosci 12:1238–1247.

Barthas F, Kwan AC (2017) Secondary motor cortex: where 'sensory' meets 'motor' in the rodent frontal cortex. Trends Neurosci 40:181–193.

Batista-Brito R, Rossignol E, Hjerling-Leffler J, Denaxa M, Wegner M, Lefebvre V, Pachnis V, Fishell G (2009) The cell-intrinsic requirement of Sox6 for cortical interneuron development. Neuron 63:466–481.

Bielle F, Griveau A, Narboux-Nême N, Vigneau S, Sigrist M, Arber S, Wassef M, Pierani A (2005) Multiple origins of cajal-retzius cells at the borders of the developing pallium. Nat Neurosci 8:1002–1012.

Boraud T, Bezard E, Guehl D, Bioulac B, Gross C (1998) Effects of L-DOPA on neuronal activity of the globus pallidus externalis (GPe) and globus pallidus internalis (GPi) in the MPTP-treated monkey. Brain Res 787: 157–160.

Butt SJ, Sousa VH, Fuccillo MV, Hjerling-Leffler J, Miyoshi G, Kimura S, Fishell G (2008) The requirement of Nkx2–1 in the temporal specification of cortical interneuron subtypes. Neuron 59:722–732.

Chan CS, Glajch KE, Gertler TS, Guzman JN, Mercer JN, Lewis AS, Goldberg AB, Tkatch T, Shigemoto R, Fleming SM, Chetkovich DM, Osten P, Kita H, Surmeier DJ (2011) HCN channelopathy in external globus pallidus neurons in models of Parkinson's disease. Nat Neurosci 14:85–92.

Chan CS, Peterson JD, Gertler TS, Glajch KE, Quintana RE, Cui Q, Sebel LE, Plotkin JL, Shen W, Heiman M, Heintz N, Greengard P, Surmeier DJ (2012) Strain-specific regulation of striatal phenotype in Drd2-eGFP BAC transgenic mice. J Neurosci 32:9124–9132.

Chen MC, Ferrari L, Sacchet MD, Foland-Ross LC, Qiu MH, Gotlib IH, Fuller PM, Arrigoni E, Lu J (2015) Identification of a direct GABAergic pallidocortical pathway in rodents. Eur J Neurosci 41:748–759.

Chittajallu R, Craig MT, McFarland A, Yuan X, Gerfen S, Tricoire L, Erkkila B, Barron SC, López CM, Liang BJ, Jeffries BW, Pelkey KA, McBain CJ (2013) Dual origins of functionally distinct O-LM interneurons revealed by differential 5-HT(3A)R expression. Nat Neurosci 16:1598–1607.

Clemente-Perez A, Makinson SR, Higashikubo B, Brovarney S, Cho FS, Urry A, Holden SS, Wimer M, Dávid C, Fenno LE, Acsády L, Deisseroth K, Paz JT (2017) Distinct thalamic reticular cell types differentially modulate normal and pathological cortical rhythms. Cell Rep 19:2130–2142.

Cornwall J, Cooper JD, Phillipson OT (1990) Projections to the rostral reticular thalamic nucleus in the rat. Exp Brain Res 80:157–171.

Cowan RL, Wilson CJ (1994) Spontaneous firing patterns and axonal projections of single corticostriatal neurons in the rat medial agranular cortex. J Neurophysiol 71:17–32.

Cox J, Witten IB (2019) Striatal circuits for reward learning and decision-making. Nat Rev Neurosci 20:482–494.

Cui Q, Pitt JE, Pamukcu A, Poulin JF, Mabrouk OS, Fiske MP, Fan IB, Augustine EC, Young KA, Kennedy RT, Awatramani R, Chan CS (2016) Blunted mGluR activation disinhibits striatopallidal transmission in parkinsonian mice. Cell Rep 17:2431–2444.

Daigle TL, Madisen L, Hage TA, Valley MT, Knoblich U, Larsen RS, Takeno MM, Huang L, Gu H, Larsen R, Mills M, Bosma-Moody A, Siverts LA, Walker M, Graybuck LT, Yao Z, Fong O, Nguyen TN, Garren E, Lenz GH, et al. (2018) A suite of transgenic driver and reporter mouse lines with enhanced brain-cell-type targeting and functionality. Cell 174:465–480.e422.

de Carlos JA, López-Mascaraque L, Valverde F (1996) Dynamics of cell migration from the lateral ganglionic eminence in the rat. J Neurosci 16:6146–6156.

DeLong MR (1971) Activity of pallidal neurons during movement. J Neurophysiol 34:414–427.

DeLong MR, Wichmann T (2007) Circuits and circuit disorders of the basal ganglia. Arch Neurol 64:20–24.

Dodson PD, Larvin JT, Duffell JM, Garas FN, Doig NM, Kessaris N, Duguid IC, Bogacz R, Butt SJ, Magill PJ (2015) Distinct developmental origins manifest in the specialized encoding of movement by adult neurons of the external globus pallidus. Neuron 86:501–513.

Du T, Xu Q, Ocbina PJ, Anderson SA (2008) NKX2.1 specifies cortical interneuron fate by activating Lhx6. Development 135:1559–1567.

Dudman JT, Krakauer JW (2016) The basal ganglia: from motor commands to the control of vigor. Curr Opin Neurobiol 37:158–166.

Economo MN, Clack NG, Lavis LD, Gerfen CR, Svoboda K, Myers EW, Chandrashekar J (2016) A platform for brain-wide imaging and reconstruction of individual neurons. eLife 5:e10566.

Filion M, Tremblay L, Bédard PJ (1991) Effects of dopamine agonists on the spontaneous activity of globus pallidus neurons in monkeys with MPTP-induced parkinsonism. Brain Res 547:152–161.

Flames N, Pla R, Gelman DM, Rubenstein JL, Puelles L, Marín O (2007) Delineation of multiple subpallial progenitor domains by the combinatorial expression of transcriptional codes. J Neurosci 27:9682–9695.

Flandin P, Kimura S, Rubenstein JL (2010) The progenitor zone of the ventral medial ganglionic eminence requires Nkx2–1 to generate most of the globus pallidus but few neocortical interneurons. J Neurosci 30:2812–2823.

Fogarty M, Grist M, Gelman D, Marín O, Pachnis V, Kessaris N (2007) Spatial genetic patterning of the embryonic neuroepithelium generates GABAergic interneuron diversity in the adult cortex. J Neurosci 27: 10935–10946.

Fox CA, Andrade AN, Lu Qui IJ, Rafols JA (1974) The primate globus pallidus: a golgi and electron microscopic study. J Hirnforsch 15:75–93.

Gandia JA, De Las Heras S, García M, Giménez-Amaya JM (1993) Afferent projections to the reticular thalamic nucleus from the globus pallidus and the substantia nigra in the rat. Brain Res Bull 32:351–358.

Gelman DM, Martini FJ, Nóbrega-Pereira S, Pierani A, Kessaris N, Marín O (2009) The embryonic preoptic area is a novel source of cortical GABAergic interneurons. J Neurosci 29:9380–9389.

Gelman D, Griveau A, Dehorter N, Teissier A, Varela C, Pla R, Pierani A, Marín O (2011) A wide diversity of cortical GABAergic interneurons derives from the embryonic preoptic area. J Neurosci 31:16570–16580.

Gerfen CR, Paletzki R, Heintz N (2013) GENSAT BAC cre-recombinase driver lines to study the functional organization of cerebral cortical and basal ganglia circuits. Neuron 80:1368–1383.

Glajch KE, Kelver DA, Hegeman DJ, Cui Q, Xenias HS, Augustine EC, Hernández VM, Verma N, Huang TY, Luo M, Justice NJ, Chan CS (2016) Npas1+ pallidal neurons target striatal projection neurons. J Neurosci 36:5472–5488.

Gorski JA, Talley T, Qiu M, Puelles L, Rubenstein JL, Jones KR (2002) Cortical excitatory neurons and glia, but not GABAergic neurons, are produced in the Emx1-expressing lineage. J Neurosci 22:6309–6314.

Gouwens NW, Sorensen SA, Berg J, Lee C, Jarsky T, Ting J, Sunkin SM, Feng D, Anastassiou CA, Barkan E, Bickley K, Blesie N, Braun T, Brouner K, Budzillo A, Caldejon S, Casper T, Castelli D, Chong P, Crichton K, et al. (2019) Classification of electrophysiological and morphological neuron types in the mouse visual cortex. Nat Neurosci 22:1182–1195.

Graybiel AM (2008) Habits, rituals, and the evaluative brain. Annu Rev Neurosci 31:359–387.

Grillner S, Robertson B (2016) The basal ganglia over 500 million years. Curr Biol 26:R1088–R1100.

Gritti I, Henny P, Galloni F, Mainville L, Mariotti M, Jones BE (2006) Stereological estimates of the basal forebrain cell population in the rat, including neurons containing choline acetyltransferase, glutamic acid decarboxylase or phosphate-activated glutaminase and colocalizing vesicular glutamate transporters. Neuroscience 143:1051–1064.

Hanks TD, Summerfield C (2017) Perceptual decision making in rodents, monkeys, and humans. Neuron 93:15–31.

Harris JA, Hirokawa KE, Sorensen SA, Gu H, Mills M, Ng LL, Bohn P, Mortrud M, Ouellette B, Kidney J, Smith KA, Dang C, Sunkin S, Bernard A, Oh SW, Madisen L, Zeng H (2014) Anatomical characterization of cre driver mice for neural circuit mapping and manipulation. Front Neural Circuits 8:76.

Harris KD, Shepherd GM (2015) The neocortical circuit: themes and variations. Nat Neurosci 18:170–181.

Hazrati LN, Parent A (1991) Projection from the external pallidum to the reticular thalamic nucleus in the squirrel monkey. Brain Res 550:142–146.

Hegeman DJ, Hong ES, Hernández VM, Chan CS (2016) The external globus pallidus: progress and perspectives. Eur J Neurosci 43:1239–1265.

Hernández VM, Hegeman DJ, Cui Q, Kelver DA, Fiske MP, Glajch KE, Pitt JE, Huang TY, Justice NJ, Chan CS (2015) Parvalbumin+ neurons and Npas1+ neurons are distinct neuron classes in the mouse external globus pallidus. J Neurosci 35:11830–11847.

Hintiryan H, Foster NN, Bowman I, Bay M, Song MY, Gou L, Yamashita S, Bienkowski MS, Zingg B, Zhu M, Yang XW, Shih JC, Toga AW, Dong HW (2016) The mouse corticostriatal projectome. Nat Neurosci 19:1100–1114.

Ho J, Tumkaya T, Aryal S, Choi H, Claridge-Chang A (2019) Moving beyond P values: data analysis with estimation graphics. Nat Methods 16:565–566.

Hooks BM, Papale AE, Paletzki RF, Feroze MW, Eastwood BS, Couey JJ, Winnubst J, Chandrashekar J, Gerfen CR (2018) Topographic precision in sensory and motor corticostriatal projections varies across cell type and cortical area. Nat Commun 9:3549.

Huang ZJ, Di Cristo G, Ango F (2007) Development of GABA innervation in the cerebral and cerebellar cortices. Nat Rev Neurosci 8:673–686.

Hunt AJ Jr, Dasgupta R, Rajamanickam S, Jiang Z, Beierlein M, Chan CS, Justice NJ (2018) Paraventricular hypothalamic and amygdalar CRF neurons synapse in the external globus pallidus. Brain Struct Funct 223:2685–2698.

Hutchison WD, Lozano AM, Davis KD, Saint-Cyr JA, Lang AE, Dostrovsky JO (1994) Differential neuronal activity in segments of globus pallidus in Parkinson's disease patients. Neuroreport 5:1533–1537.

Ito M, Doya K (2011) Multiple representations and algorithms for reinforcement learning in the corticobasal ganglia circuit. Curr Opin Neurobiol 21:368–373.

Iwamuro H, Tachibana Y, Ugawa Y, Saito N, Nambu A (2017) Information processing from the motor cortices to the subthalamic nucleus and globus pallidus and their somatotopic organizations revealed electrophysiologically in monkeys. Eur J Neurosci 46:2684–2701.

Jaeger D, Kita H (2011) Functional connectivity and integrative properties of globus pallidus neurons. Neuroscience 198:44–53.

Jaglin XH, Hjerling-Leffler J, Fishell G, Batista-Brito R (2012) The origin of neocortical nitric oxide synthase-expressing inhibitory neurons. Front Neural Circuits 6:44.

Jahanshahi M, Obeso I, Rothwell JC, Obeso JA (2015) A fronto-striato-subthalamic-pallidal network for goal-directed and habitual inhibition. Nat Rev Neurosci 16:719–732.

Jeong M, Kim Y, Kim J, Ferrante DD, Mitra PP, Osten P, Kim D (2016) Comparative three-dimensional connectome map of motor cortical projections in the mouse brain. Sci Rep 6:20072.

Jiménez D, López-Mascaraque LM, Valverde F, De Carlos JA (2002) Tangential migration in neocortical development. Dev Biol 244:155–169.

Jin X, Tecuapetla F, Costa RM (2014) Basal ganglia subcircuits distinctively encode the parsing and concatenation of action sequences. Nat Neurosci 17:423–430.

Kanki H, Suzuki H, Itohara S (2006) High-efficiency CAG-FLPe deleter mice in C57BL/6J background. Exp Anim 55:137–141.

Karube F, Takahashi S, Kobayashi K, Fujiyama F (2019) Motor cortex can directly drive the globus pallidal neurons in a projection neuron type dependent manner in rat. Elife 8:pii: e49511.

Kawaguchi Y (2017) Pyramidal cell subtypes and their synaptic connections in layer 5 of rat frontal cortex. Cereb Cortex 27:5755–5771.

Kayahara T, Nakano K (1998) The globus pallidus sends axons to the thalamic reticular nucleus neurons projecting to the centromedian nucleus of the thalamus: a light and electron microscope study in the cat. Brain Res Bull 45:623–630.

Kim Y, Yang GR, Pradhan K, Venkataraju KU, Bota M, García Del Molino LC, Fitzgerald G, Ram K, He M, Levine JM, Mitra P, Huang ZJ, Wang XJ, Osten P (2017) Brain-wide maps reveal stereotyped cell-type-based cortical architecture and subcortical sexual dimorphism. Cell 171:456-469.e22.

Kita H (2007) Globus pallidus external segment. Prog Brain Res 160:111–133.

Kita T, Kita H (2012) The subthalamic nucleus is one of multiple innervation sites for long-range corticofugal axons: a single-axon tracing study in the rat. J Neurosci 32:5990–5999.

Klaus A, Alves da Silva J, Costa RM (2019) What, if, and when to move: basal ganglia circuits and self-paced action initiation. Annu Rev Neurosci 42:459–483.

Knowland D, Lilascharoen V, Pacia CP, Shin S, Wang EH, Lim BK (2017) Distinct ventral pallidal neural populations mediate separate symptoms of depression. Cell 170:284–297.e18.

Krzywinski M, Altman N (2014) Visualizing samples with box plots. Nat Methods 11:119–120.

Liodis P, Denaxa M, Grigoriou M, Akufo-Addo C, Yanagawa Y, Pachnis V (2007) Lhx6 activity is required for the normal migration and specification of cortical interneuron subtypes. J Neurosci 27:3078–3089.

Magill PJ, Bolam JP, Bevan MD (2001) Dopamine regulates the impact of the cerebral cortex on the subthalamic nucleus-globus pallidus network. Neuroscience 106:313–330.

Mallet N, Pogosyan A, Márton LF, Bolam JP, Brown P, Magill PJ (2008) Parkinsonian beta oscillations in the external globus pallidus and their relationship with subthalamic nucleus activity. J Neurosci 28:14245–14258.

Mallet N, Schmidt R, Leventhal D, Chen F, Amer N, Boraud T, Berke JD (2016) Arkypallidal cells send a stop signal to striatum. Neuron 89:308–316.

Mandelbaum G, Taranda J, Haynes TM, Hochbaum DR, Huang KW, Hyun M, Umadevi Venkataraju K, Straub C, Wang W, Robertson K, Osten P, Sabatini BL (2019) Distinct cortical-thalamic-striatal circuits through the parafascicular nucleus. Neuron 102:636–652.e7.

Mastro KJ, Bouchard RS, Holt HA, Gittis AH (2014) Transgenic mouse lines subdivide external segment of the globus pallidus (GPe) neurons and reveal distinct GPe output pathways. J Neurosci 34:2087–2099.

Mastro KJ, Zitelli KT, Willard AM, Leblanc KH, Kravitz AV, Gittis AH (2017) Cell-specific pallidal intervention induces long-lasting motor recovery in dopamine-depleted mice. Nat Neurosci 20:815–823.

Metsalu T, Vilo J (2015) ClustVis: a web tool for visualizing clustering of multivariate data using principal component analysis and heatmap. Nucleic Acids Res 43:W566–W570.

Milardi D, Gaeta M, Marino S, Arrigo A, Vaccarino G, Mormina E, Rizzo G, Milazzo C, Finocchio G, Baglieri A, Anastasi G, Quartarone A (2015) Basal ganglia network by constrained spherical deconvolution: a possible corticopallidal pathway? Mov Disord 30:342–349.

Mink JW (2018) Basal ganglia mechanisms in action selection, plasticity, and dystonia. Eur J Paediatr Neurol 22:225–229.

Moriizumi T, Hattori T (1992) Separate neuronal populations of the rat globus pallidus projecting to the subthalamic nucleus, auditory cortex and pedunculopontine tegmental area. Neuroscience 46:701–710.

Naito A, Kita H (1994) The corticopallidal projection in the rat: an anterograde tracing study with biotinylated dextran amine. Brain Res 653:251–257.

Nakajima M, Schmitt LI, Halassa MM (2019) Prefrontal cortex regulates sensory filtering through a basal ganglia-to-thalamus pathway. Neuron 103:445–458.e10.

Nambu A, Tachibana Y (2014) Mechanism of parkinsonian neuronal oscillations in the primate basal ganglia: some considerations based on our recent work. Front Syst Neurosci 8:74.

Nambu A, Tokuno H, Hamada I, Kita H, Imanishi M, Akazawa T, Ikeuchi Y, Hasegawa N (2000) Excitatory cortical inputs to pallidal neurons via the subthalamic nucleus in the monkey. J Neurophysiol 84:289–300.

Nini A, Feingold A, Slovin H, Bergman H (1995) Neurons in the globus pallidus do not show correlated activity in the normal monkey, but phase-

locked oscillations appear in the MPTP model of parkinsonism. J Neurophysiol 74:1800–1805.

Nóbrega-Pereira S, Kessaris N, Du T, Kimura S, Anderson SA, Marín O (2008) Postmitotic Nkx2–1 controls the migration of telencephalic interneurons by direct repression of guidance receptors. Neuron 59:733–745.

Nóbrega-Pereira S, Gelman D, Bartolini G, Pla R, Pierani A, Marín O (2010) Origin and molecular specification of globus pallidus neurons. J Neurosci 30:2824–2834.

Oh YM, Karube F, Takahashi S, Kobayashi K, Takada M, Uchigashima M, Watanabe M, Nishizawa K, Kobayashi K, Fujiyama F (2017) Using a novel PV-cre rat model to characterize pallidonigral cells and their terminations. Brain Struct Funct 222:2359–2378.

Papale AE, Hooks BM (2018) Circuit changes in motor cortex during motor skill learning. Neuroscience 368:283–297.

Parent A, Boucher R, O'Reilly-Fromentin J (1981) Acetylcholinesterase-containing neurons in cat pallidal complex; morphological characteristics and projection towards the neocortex. Brain Res 230:356–361.

Pasquereau B, Turner RS (2011) Primary motor cortex of the parkinsonian monkey: differential effects on the spontaneous activity of pyramidal tract-type neurons. Cereb Cortex 21:1362–1378.

Pazo JH, Barceló AC, Bellantonio E, Pazo VC, Almarares N (2013) Electrophysiologic study of globus pallidus projections to the thalamic reticular nucleus. Brain Res Bull 94:82–89.

Pennartz CM, Berke JD, Graybiel AM, Ito R, Lansink CS, van der Meer M, Redish AD, Smith KS, Voorn P (2009) Corticostriatal interactions during learning, memory processing, and decision making. J Neurosci 29:12831–12838.

Poulin JF, Caronia G, Hofer C, Cui Q, Helm B, Ramakrishnan C, Chan CS, Dombeck DA, Deisseroth K, Awatramani R (2018) Mapping projections of molecularly defined dopamine neuron subtypes using intersectional genetic approaches. Nat Neurosci 21:1260–1271.

Raz A, Vaadia E, Bergman H (2000) Firing patterns and correlations of spontaneous discharge of pallidal neurons in the normal and the tremulous 1-methyl-4-phenyl-1,2,3,6-tetrahydropyridine vervet model of parkinsonism. J Neurosci 20:8559–8571.

Redgrave P, Rodriguez M, Smith Y, Rodriguez-Oroz MC, Lehericy S, Bergman H, Agid Y, DeLong MR, Obeso JA (2010) Goal-directed and habitual control in the basal ganglia: implications for Parkinson's disease. Nat Rev Neurosci 11:760–772.

Rothblat DS, Schneider JS (1995) Alterations in pallidal neuronal responses to peripheral sensory and striatal stimulation in symptomatic and recovered parkinsonian cats. Brain Res 705:1–14.

Rubenstein JL, Shimamura K, Martinez S, Puelles L (1998) Regionalization of the prosencephalic neural plate. Annu Rev Neurosci 21:445–477.

Saunders A, Oldenburg IA, Berezovskii VK, Johnson CA, Kingery ND, Elliott HL, Xie T, Gerfen CR, Sabatini BL (2015) A direct GABAergic output from the basal ganglia to frontal cortex. Nature 521:85–89.

Saunders A, Macosko EZ, Wysoker A, Goldman M, Krienen FM, de Rivera H, Bien E, Baum M, Bortolin L, Wang S, Goeva A, Nemesh J, Kamitaki N, Brumbaugh S, Kulp D, McCarroll SA (2018) Molecular diversity and specializations among the cells of the adult mouse brain. Cell 174:1015–1030.e16.

Schindelin J, Arganda-Carreras I, Frise E, Kaynig V, Longair M, Pietzsch T, Preibisch S, Rueden C, Saalfeld S, Schmid B, Tinevez JY, White DJ, Hartenstein V, Eliceiri K, Tomancak P, Cardona A (2012) Fiji: an open-source platform for biological-image analysis. Nat Methods 9:676–682.

Schwarz LA, Miyamichi K, Gao XJ, Beier KT, Weissbourd B, DeLoach KE, Ren J, Ibanes S, Malenka RC, Kremer EJ, Luo L (2015) Viral-genetic tracing of the input-output organization of a central noradrenaline circuit. Nature 524:88–92.

Shammah-Lagnado SJ, Alheid GF, Heimer L (1996) Efferent connections of the caudal part of the globus pallidus in the rat. J Comp Neurol 376:489–507.

Shepherd GM (2014) Diversity and complexity in the pyramidal tract projectome. Nat Rev Neurosci 15:63.

Sherman SM (2016) Thalamus plays a central role in ongoing cortical functioning. Nat Neurosci 19:533–541.

Shi LH, Luo F, Woodward DJ, Chang JY (2004) Neural responses in multiple basal ganglia regions during spontaneous and treadmill locomotion tasks in rats. Exp Brain Res 157:303–314.

Shibata KI, Tanaka T, Hioki H, Furuta T (2018) Projection patterns of corticofugal neurons associated with vibrissa movement. eNeuro 5:ENEURO.0190-18.2018.

Silberberg SN, Taher L, Lindtner S, Sandberg M, Nord AS, Vogt D, McKinsey GL, Hoch R, Pattabiraman K, Zhang D, Ferran JL, Rajkovic A, Golonzhka O, Kim C, Zeng H, Puelles L, Visel A, Rubenstein JLR (2016) Subpallial enhancer transgenic lines: a data and tool resource to study transcriptional regulation of GABAergic cell fate. Neuron 92:59–74.

Smith Y, Wichmann T (2015) The corticopallidal projection: an additional route for cortical regulation of the basal ganglia circuitry. Mov Disord 30:293–295.

Streit M, Gehlenborg N (2014) Bar charts and box plots. Nat Methods 11:117.

Sun Q, Li X, Ren M, Zhao M, Zhong Q, Ren Y, Luo P, Ni H, Zhang X, Zhang C, Yuan J, Li A, Luo M, Gong H, Luo Q (2019) A whole-brain map of long-range inputs to GABAergic interneurons in the mouse medial prefrontal cortex. Nat Neurosci 22:1357–1370.

Sussel L, Marín O, Kimura S, Rubenstein JL (1999) Loss of Nkx2.1 homeobox gene function results in a ventral to dorsal molecular respecification within the basal telencephalon: evidence for a transformation of the pallidum into the striatum. Development 126:3359–3370.

Svoboda K, Li N (2018) Neural mechanisms of movement planning: motor cortex and beyond. Curr Opin Neurobiol 49:33–41.

Tamamaki N, Fujimori KE, Takauji R (1997) Origin and route of tangentially migrating neurons in the developing neocortical intermediate zone. J Neurosci 17:8313–8323.

Turner RS, Anderson ME (2005) Context-dependent modulation of movement-related discharge in the primate globus pallidus. J Neurosci 25:2965–2976.

Van der Kooy D, Kolb B (1985) Non-cholinergic globus pallidus cells that project to the cortex but not to the subthalamic nucleus in rat. Neurosci Lett 57:113–118.

Wamsley B, Fishell G (2017) Genetic and activity-dependent mechanisms underlying interneuron diversity. Nat Rev Neurosci 18:299–309.

Wichmann T, Delong MR (2006) Deep brain stimulation for neurologic and neuropsychiatric disorders. Neuron 52:197–204.

Wichmann T, Bergman H, DeLong MR (2018) Basal ganglia, movement disorders and deep brain stimulation: advances made through non-human primate research. J Neural Transm 125:419–430.

Xu Q, Tam M, Anderson SA (2008) Fate mapping Nkx2.1-lineage cells in the mouse telencephalon. J Comp Neurol 506:16–29.

Yetman MJ, Washburn E, Hyun JH, Osakada F, Hayano Y, Zeng H, Callaway EM, Kwon HB, Taniguchi H (2019) Intersectional monosynaptic tracing for dissecting subtype-specific organization of GABAergic interneuron inputs. Nat Neurosci 22:492–502.

Zeisel A, Hochgerner H, Lönnerberg P, Johnsson A, Memic F, van der Zwan J, Haring M, Braun E, Borm LE, La Manno G, Codeluppi S, Furlan A, Lee K, Skene N, Harris KD, Hjerling-Leffler J, Arenas E, Ernfors P, Marklund U, Linnarsson S (2018) Molecular architecture of the mouse nervous system. Cell 174:999–1014.e22.